NORTHWESTERN UNIVERSITY

Shift-Invariant Real-Time High-Speed Optical Image Correlation System

A DISSERTATION

SUBMITTED TO THE GRADUATE SCHOOL IN PARTIAL FULFILLMENT OF THE REQUIREMENTS

for the degree

DOCTOR OF PHILOSOPHY

Field of Electrical Engineering

By

Alexander Heifetz

EVANSTON, ILLINOIS

September 2005

Abstract

We have studied, theoretically as well as experimentally, diffraction from volume holographic gratings, and its application to design of optical image correlation system. We have investigated a holographic system for image recognition in real time by implementing a time-efficient exhaustive search in a very large image database with a shift-invariant correlator. Our system has the potential of achieving correlation data processing rate of 10^{12} bps. The database of filter images contains multiple copies of the same image to account for rotation and scale variance, while shift invariance is accomplished by using a thin correlator material. The filter images are to be stored in the ultra-high density spatio-angular multiplexed holographic memory with nearly 2TB storage capacity. Real-time recognition of the stream of the incoming query images is performed with a photorefractive holographic correlator. Time-efficient search is accomplished if one uses a real-time VanderLugt correlator, because this architecture allows to overcome the speed limit of the photorefractive gratings formation. For the preliminary experiments, we constructed edge-enhanced VanderLugt-type spatial filters using samples of 6μm thick silver-halide emulsion layer deposited on a glass surface. These samples possessed the shit-invariance properties; however because these materials produced permanent holographic recordings, they were not suitable for real-time operation. We identified photorefractive polymers that can be made as thin as 16μm, and as a consequence posses a large degree of shift-invariance, to be the best materials for real-time correlation. Photorefractive polymers were discovered rather recently, and their properties are currently under active investigation. We performed a series of

experiments to measure the angular bandwidth of these materials in the phase conjugation process by a degenerate four-wave mixing arrangement. We also demonstrated shift-invariant correlation in the real-time VanderLugt architecture using this material. In addition, we investigated theoretically and experimentally the direction of the diffracted beam for off-Bragg incidence. This analysis is important in designing an actual working optical correlator system, since one must be able to predict the direction of the correlation beam. The work performed under this thesis project has thus established the feasibility of a real-time, high-speed, translation-invariant image identification system. Future work would center on engineering optimization of this artificial vision technology.

Acknowledgments

I would like to thank the people who have contributed to this thesis. I especially thank my thesis advisor, Professor Selim Shahriar, for introducing me to the field of optics. Special thanks also go to the members of the thesis committee, Professors Allen Taflove and Thrasos Pappas for their patient advice and suggestions.

I wish to thank the many students, post-docs and visitors at the Center for Photonic Communication and Computing at Northwestern. I especially thank Gour Pati whose assistance was invaluable. I also thank John Shen, Jong-Kwon Lee, Joe Vornehm, Ken Salit, Mary Messal, George Cardoso, Renu Tripathi, Venkatesh Gopal and Prabhakar Pradhan for their cooperation in various aspects of my graduate studies.

I also thank my fiancé Inna who has been the source of my inspiration. I also want to thank my mother for years of support and encouragement.

Contents

List of Figures

Shift-Invariant Real-Time High-Speed Optical Image Correlation System

We have studied, theoretically as well as experimentally, diffraction from volume holographic gratings, and its application to design of optical image correlation system. We have investigated a holographic system for image recognition in real time by implementing a time-efficient exhaustive search in a very large image database with a shift-invariant correlator. Our system has the potential of achieving correlation data processing rate of 10^{12} bps. The database of filter images contains multiple copies of the same image to account for rotation and scale variance, while shift invariance is accomplished by using a thin correlator material. The filter images are to be stored in the ultra-high density spatio-angular multiplexed holographic memory with nearly 2TB storage capacity. Real-time recognition of the stream of the incoming query images is performed with a photorefractive holographic correlator. Time-efficient search is accomplished if one uses a real-time VanderLugt correlator, because this architecture allows to overcome the speed limit of the photorefractive gratings formation. For the preliminary experiments, we constructed edge-enhanced VanderLugt-type spatial filters using samples of 6μm thick silver-halide emulsion layer deposited on a glass surface. These samples possessed the shit-invariance properties; however because these materials produced permanent holographic recordings, they were not suitable for real-time operation. We identified photorefractive polymers that can be made as thin as 16μm, and as a consequence posses a large degree of shift-invariance, to be the best materials for real-time correlation. Photorefractive polymers were discovered rather recently, and their properties are currently under active investigation. We performed a series of

experiments to measure the angular bandwidth of these materials in the phase conjugation process by a degenerate four-wave mixing arrangement. We also demonstrated shift-invariant correlation in the real-time VanderLugt architecture using this material. In addition, we investigated theoretically and experimentally the direction of the diffracted beam for off-Bragg incidence. This analysis is important in designing an actual working optical correlator system, since one must be able to predict the direction of the correlation beam. The work performed under this thesis project has thus established the feasibility of a real-time, high-speed, translation-invariant image identification system. Future work would center on engineering optimization of this artificial vision technology.

1 Introduction

1.1 Historical Developments of Holography and Optical Correlation

In holography two coherent light waves are overlapped to create an interference pattern as in Figure 1(a). A hologram is formed when an appropriate material is placed in the fringe pattern of light and darkness (shown by dark horizontal lines in Figure 1(a)), which leaves a corresponding pattern imprint on the refractive index of the material. The pattern created has the special property that if one of the light waves responsible for it is incident on the hologram, then some of the light from that wave is diffracted to recreate the detail of the wavefronts of the second wave. This is why images with depth are observed from holograms. The reconstruction process is shown in Figure 1(b).

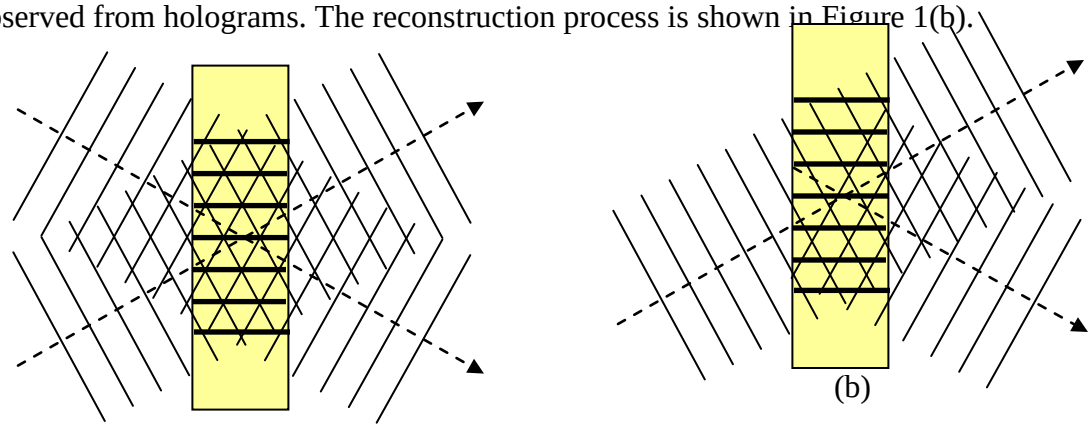

Figure 1. Holographic Principle (a) Recording of a hologram. (b) Wavefront reconstruction.

Holography dates from 1947, when British/Hungarian scientist Dennis Gabor developed the theory of holography while working to improve the resolution of an electron microscope [1]. Gabor, who characterized his work as “an experiment in serendipity” that was “begun too soon,” coined the term hologram from the Greek words *holos*, meaning “whole,” and *gramma*, meaning “message.” In 1971, Gabor was awarded the Nobel Prize in Physics for his discovery of holography. Gabor’s holography was limited to film transparencies using a mercury arc lamp as the light source, which in those early years was the most coherent light source. Because of the low coherency of this light, it was not possible to produce holograms at any depth. Gabor’s holograms contained distortions and an extraneous twin image. Further development in the field was stymied for the next decade because of the lack of coherent light sources.

This barrier was overcome in 1960 with the invention of the laser by Prokhorov and Basov in the USSR and Towens in the USA. The laser beams possessed the qualities, such as high intensity and long coherence length, which were ideal for writing holograms. For the next ten years, the field of holography and its applications mushroomed. In 1962 Emmett Leith and Juris Upatnieks of the University of

Michigan read Gabor's paper and decided to duplicate Gabor's technique using the laser and an "off-axis" technique borrowed from their work in the development of side-reading radar [2]. The result was the first laser transmission hologram of 3-D objects (a toy train and a bird) [3]. The pioneering work of Leith and Upatnieks led to the standardization of the equipment used to make holograms, i.e., a CW laser, optical devices (lens, mirrors and beam splitters) for directing laser light, a film holder and an isolation table on which exposures are made. Stability is absolutely essential because vibration as small as quarter wavelength of light during exposures can completely spoil the hologram.

The field of optical correlation received a major boost in 1964 when A.B. VanderLugt of the University of Michigan published a paper in which he described an optical implementation of matched filtering, since then called a VanderLugt correlator [4]. In 1967 C.J. Weaver and J.W. Goodman of Stanford University invented a joint-transform correlator [5]. However, the experimental implementation of an optical correlator system was suffering from the lack of appropriate materials. In the 60s, holograms were in write-once materials, which were typically silver halide emulsions or dichromated gelatin. The implementation of correlators required a two-step process of recording and readout. Wet processing was normally required to develop the holograms. Once used, the holographic material had to be discarded because holograms could not be re-written in the same material.

It was soon discovered that using photorefractive effect it was possible in certain materials to write and re-write holograms an arbitrary number of times, without the need for hologram development in a separate step. The photorefractive effect was first discovered in 1966 by A. Ashkin and his colleagues at Bell Labs when they were studying the transmission of laser beams through electro-optic crystals. It was found that the presence of laser beams inside some electro-optic crystals leads to an index inhomogeneity that distorts the wavefront of the transmitted laser beam. Such an effect was referred to as "optical damage" [6]. The photorefractive effect has since been observed in many electro-optic crystals, such as $LiNbO_3$, $KNbO_3$, $BaTiO_3$, $Bi_{12}SiO_{20}$, just to name a few. N.V. Kukhtarev and his collaborators in the Soviet Union developed the first succesfull theoretical explanation of the photorefractive effect using band-transport model of impurity-doped electro-optic crystals in 1979 [7,8]. In 1969, Herwig Kogelnik, working at Bell Labs, published his landmark paper in which he developed diffraction theory from thick holographic gratings using the formalism of coupled-wave theory [9]. This was a generic diffraction theory that could be applied to any holographic gratings, regardless of the physical mechanism of their formation.

Holography received additional impetus after the phenomena of phase conjugation was discovered by B. Zel'dovich in the USSR in 1972 [10]. In 1978 Amnon Yariv at Caltech suggested to combined phase conjugation by degenerate four-wave mixing with optical correlation techniques to produce real-time photorefractive correlators with updatable holographic filters [11,12]. However, the difficult crystal growth and sample preparation required for inorganic crystals has limited the widespread of these applications. The search for new real-time holographic materials continued. In 1991, the photorefractive effect was observed for the first time in a polymer by a group led by W.E. Moerner, then at IBM [13].

The first real-time optical correlator

utilizing a photorefractive polymer was demonstrated by the University of Arizona group in 1995 [14].

1.2 Contents of Thesis

In chapter 2 we review the main results of the scalar diffraction theory, such as the Fourier transforming properties of thin lenses and the 4-f imaging system. In chapter 3 we review the basic holographic principles and also introduce the criteria for distinguishing between Bragg and Raman-Nath diffraction regimes. In chapter 4 we establish the equivalence between real-time holography and four-wave mixing, and desribe the principles of real-time VanderLugt and joint transform correlators. In chapter 5 we review the principles of photorefractive effect in organic polymer materials. In chapters 6 and 7 we introduce the two main theories for the diffraction from holographic gratings, that until now were believed to be equivalent. In chapter 6 we introduce volume diffraction in the Born approximation and show that the results of this theory are consistent with conservaion of momentum and energy laws. In chapter 7 we present coupled wave theory for thick holographic gratings, and show for the first time, that the results of this theory are not consistent with conservations of energy and momentum. In chapter 8 we describe the proposed image recognition device, consisting of super-parallel holographic memory and a shift-invariant real-time VanderLugt correlator. In chapter 9 we describe the experiment designed to measure the angular bandwidth of our photorefractive polymer samples. In chapter 10 we describe the experimental demonstration of shift-invariant real-time VanderLugt correlator implemented with a photorefractive polymer sample. Finally, chapter 11 contains the summary and

proposals for future work.

2 Scalar Diffraction Theory

In this chapter we will present key results from the scalar diffraction theory needed for developing the theory of optical signal processing [15-17]. We consider paraxial monochromatic light waves, which is a very close approximation of the Gaussian laser beams used in the optical signal processing experiments. By paraxial waves we mean waves with the k-vector that points essentially along the axis of propagation (call it *z*-axis), or equivalently $k_z >> k_\perp$. The electric field associated with a polarized monochromatic wave can be written as $u(\boldsymbol{r},t) = \mathrm{Re}[U(\boldsymbol{r})e^{j\omega t}]$, where, for example, if the field is *x*-polarized $\boldsymbol{e}(\boldsymbol{r},t) = \hat{\boldsymbol{x}}u(\boldsymbol{r},t)$. In the above equation $U(\boldsymbol{r})$ is a complex function of the spatial coordinate $\boldsymbol{r}$, and has been normalized such that the intensity associated with the monochromatic scalar wave is given by $I(\boldsymbol{r}) = |U(\boldsymbol{r})|^2$.

2.1 Fresnel Diffraction

In optical signal processing, information is encoded in the complex field envelope $U(\boldsymbol{\rho}) = U(\boldsymbol{r})|_{z=const}$, where $\boldsymbol{\rho} = (x, y)$ is the transverse plane. That is, $U(\boldsymbol{\rho})$ is the field envelope $U(\boldsymbol{r})$ in the transverse plane with the *z*-coordinated held constant (Figure 2). We need to know how does $U(\boldsymbol{\rho})$ change as the beam propagates through free space, and how can we modulate $U(\boldsymbol{\rho})$ with simple optical elements. Since free-space propagation is governed by the Helmholtz equation, which is linear and shift-invariant, free-space propagation can be solved using methods of linear system theory. Introducing the concept of a transfer function will help in understanding of the interaction of light

beams with thin optical elements.

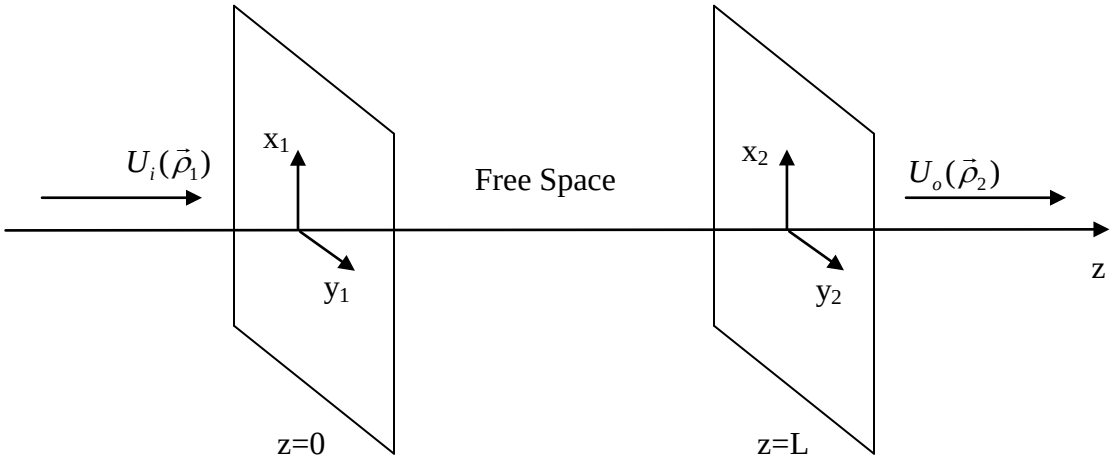

Figure 2. Free space propagation in the paraxial approximation.

In the language of linear system theory, the output field can be related to the input field via the two-dimensional convolution integral

$$U_o(\boldsymbol{\rho}_2) = \int_{-\infty}^{\infty} d\boldsymbol{\rho}_1 U_i(\boldsymbol{\rho}_1) h(\boldsymbol{\rho}_2 - \boldsymbol{\rho}_1) \tag{1}$$

where $h(\boldsymbol{\rho}_2 - \boldsymbol{\rho}_1)$ represents the impulse (point source) response of the system. In many cases, the output field can be calculated much more easily by working in the Fourier domain. The spatial Fourier transform of a 2-dimensional function $U(\boldsymbol{\rho})$ is defined as

$$\tilde{U}(\boldsymbol{f}) \equiv \int_{-\infty}^{\infty} d\boldsymbol{\rho} U(\boldsymbol{\rho}) e^{-j2\pi \boldsymbol{f}\cdot\boldsymbol{\rho}} \tag{2}$$

where $\boldsymbol{f} = (f_x, f_y)$ is a 2-dimensional spatial frequency vector. One can identify the spatial frequencies with the wavevector of a plane wave as $k_x = 2\pi f_x$, $k_y = 2\pi f_y$, and

$k_z = 2\pi\sqrt{(\nu/c)^2 - f_x^2 - f_y^2}$. $U(\boldsymbol{\rho})$ can be recovered from $\tilde{U}(\boldsymbol{f})$ by the inverse Fourier transformation defined via

$$U(\boldsymbol{\rho}) \equiv \int_{-\infty}^{\infty} d\boldsymbol{f}\tilde{U}(\boldsymbol{f})e^{j2\pi\boldsymbol{f}\cdot\boldsymbol{\rho}} \tag{3}$$

In the Fourier domain,

$$\tilde{U}_o(\boldsymbol{f}) = \tilde{h}(\boldsymbol{f})\tilde{U}_i(\boldsymbol{f}) \tag{4}$$

In free space, under paraxial approximation, in the Fourier domain

$$\tilde{h}(\boldsymbol{f}) = e^{jkL}e^{-j\pi\lambda L|\boldsymbol{f}|^2} \tag{5}$$

and in the spatial domain

$$h(\boldsymbol{\rho}) = \frac{e^{jkL}}{j\lambda L}e^{jk|\boldsymbol{\rho}|^2/2L} \tag{6}$$

A key result obtained in the scalar diffraction theory is the Fresnel diffraction formula

$$U_o(\boldsymbol{\rho}_2) = \frac{e^{jkL}}{j\lambda L}\int_{-\infty}^{\infty} d\boldsymbol{\rho}_1 U_i(\boldsymbol{\rho}_1)e^{jk|\boldsymbol{\rho}_2-\boldsymbol{\rho}_1|^2/2L} \tag{7}$$

It gives, under paraxial approximation, the output field $U_o(\boldsymbol{\rho}_2)$ in terms of the input field $U_i(\boldsymbol{\rho}_1)$ as a 2-dimensional integral over the input plane. The quantity $\frac{e^{jkL}}{L}e^{jk|\boldsymbol{\rho}_2-\boldsymbol{\rho}_1|^2/2L}$ is a spherical wavefront due to a point source in the paraxial approximation. Therefore, the Fresnel diffraction is essentially a statement of the Huygens principle, which says that every point on the wavefront acts as a source generating new waves.

The Fresnel diffraction integral can be written as

$$U_o(\boldsymbol{\rho}_2) = \frac{e^{jk(L+|\boldsymbol{\rho}_2|^2/2L)}}{j\lambda L}\tilde{U}_i'(\boldsymbol{f})\,|_{\boldsymbol{f}=\boldsymbol{\rho}_2/\lambda L} \tag{8}$$

where $U_i'(\boldsymbol{\rho}_1) \equiv e^{jk|\boldsymbol{\rho}_1|^2/2L}U_i(\boldsymbol{\rho}_1)$. If the propagation distance L is large enough, one can make the so-called far field or Fraunhofer approximation $k\,|\,\boldsymbol{\rho}_1\,|^2/2L \approx 0$. The output field takes on the form

$$U_o(\boldsymbol{\rho}_2) = \frac{e^{jk(L+|\boldsymbol{\rho}_2|^2/2L)}}{j\lambda L}\tilde{U}_i(\boldsymbol{\rho}_2/\lambda L) \tag{9}$$

which is known as the Fraunhofer diffraction formula.

2.2 Fourier-Transforming Properties of a Thin Lens

The action of a thin positive lens on a $+z$ propagating light beam (sketched in Figure 3) can be described by a complex transmittance function $t(\boldsymbol{\rho})$, which relates the complex envelope $U_a(\boldsymbol{\rho})$ of the transmitted beam to the envelope $U_b(\boldsymbol{\rho})$ of the incident beam via

$$U_a(\boldsymbol{\rho}) = t(\boldsymbol{\rho})U_b(\boldsymbol{\rho}) \tag{10}$$

The fact that the above relation is local is a direct consequence of our assumption of a thin lens. The field $U_a(\boldsymbol{\rho})$ after the lens at a transverse point $\boldsymbol{\rho}$ is related only to the electric field $U_b(\boldsymbol{\rho})$ before the lens at the same transverse point. In other words, the lens is so thin that negligible diffraction effects occur in propagation from one side of the lens to the other. This is the case for lenses used in laboratory experiments.

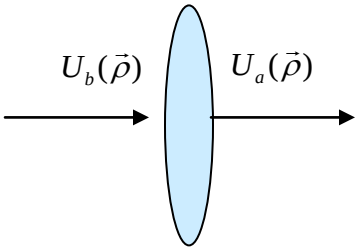

Figure 3. Model of optical transmission through a thin lens.

The transmittance function can be evaluated purely from geometrical considerations. Since the lens material is transparent, $|t(\boldsymbol{\rho})|=1$, and thus $t(\boldsymbol{\rho}) = e^{jk\eta(\boldsymbol{\rho})}$, where $\eta(\boldsymbol{\rho})$ is the optical path of light in passage through the lens at $\boldsymbol{\rho}$. One can derive the thin lens transmittance function as

$$t(\boldsymbol{\rho}) = e^{-jk|\boldsymbol{\rho}|^2/2f_l} \tag{11}$$

where f_l is the focal length of the lens. If we place such a lens just to the right of the input plane at *z=0*, then in the output plane $z = f_l$ (see Figure 4), we derive from the Fresnel diffraction formula

$$U_o(\boldsymbol{\rho}_2) = \frac{e^{jk(f_l+|\boldsymbol{\rho}_2|^2/2f_l)}}{j\lambda f_l}\tilde{U}_i(\boldsymbol{\rho}_2/\lambda f_l) \tag{12}$$

which is nothing but the Fraunhofer diffraction formula. Note that the far-field approximation was not needed to arrive at this result. The lens transmittance function exactly cancels the term that is negligible in the far-field limit.

Figure 4. Fourier transform is produced in the back focal plane of the lens.

The expression (12) contains an undesirable phase factor $e^{jk|\boldsymbol{\rho}_2|^2/2f_l}$. It turns out that the Fourier transform of the input field without the phase factors appears in the $z = 2f_l$ plane, which is the right focal plane of a Fourier transforming lens (FTL) (see Figure 5). The extra phase factor in (12) is exactly cancelled out by the phase of the free-space transfer function for propagation over distance equal to f_l. Thus we obtain

$$U_o(\boldsymbol{\rho}_2) = \frac{e^{j2kf_l}}{j\lambda f_l}\tilde{U}_i(\boldsymbol{\rho}_2/\lambda f_l) \tag{13}$$

Apart from the constant phase factor $-je^{j2kf_l}$ and scaling by λf_l, the field in the $z = 2f_l$ plane is the Fourier transform of the input field.

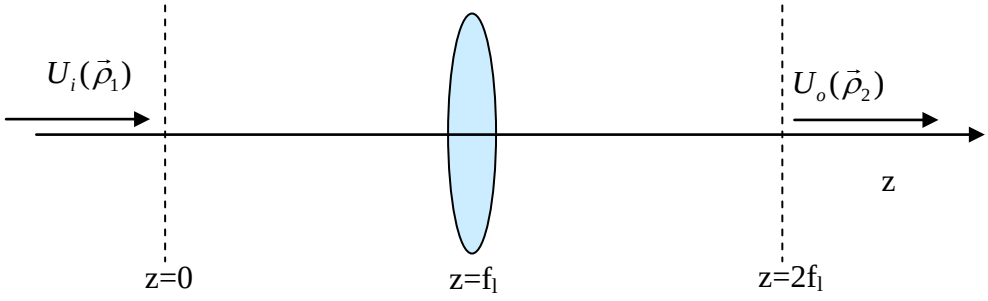

Figure 5 Fourier transform without extra phase factors

2.3 4-f Optical Imaging System

We now introduce a 4-f imaging system, which is one of the key concepts in optical signal processing. The system is sketched in Figure 6. The input field $U_i(\boldsymbol{\rho}_1)$ that we would like to optically process, exists in the z=0 plane. The field $U_i(\boldsymbol{\rho}_1)$ propagates in free space until it encounters the FTL of focal length f_l placed at $z = f_l$. The Fourier transform of the input field appears in the $z = 2f_l$. A spatial filter, such as a thin hologram, may be placed in the $z = 2f_l$ plane. We describe the spatial content of the filter with a transmittance function $t(\boldsymbol{\rho})$. Just as in the case of a thin lens, the optical field $U_b(\boldsymbol{\rho})$ before the spatial filter is related to the field $U_a(\boldsymbol{\rho})$ after the spatial filter by a local relation $U_a(\boldsymbol{\rho}) = t(\boldsymbol{\rho})U_b(\boldsymbol{\rho})$. The optical field is propagating to an inverse Fourier-transforming lens (IFTL), also of focal length f_l, placed at $z = 3f_l$. If there is no spatial filter in the $z = 2f_l$ plane, the field $U_o(\boldsymbol{\rho}_2)$ in the output plane at $z = 4f_l$ is

$$U_o(\boldsymbol{\rho}_2) = -e^{j4kf_l}U_i(-\boldsymbol{\rho}_2) \tag{14}$$

That is, aside from the constant factor $-e^{j4kf_l}$, we obtain in the output plane the inverted input field without any diffraction effects. This is to be expected since $\mathcal{F}(\mathcal{F}(f(x)) = f(-x)$, where $\mathcal{F}$ is the spatial Fourier Transform.

If there is a transparency in the $z = 2f_l$ plane with transmittance function $t(\boldsymbol{\rho})$, the field in the output plane is

$$U_o(\boldsymbol{\rho}_2) = -e^{j4kf_l}[\tilde{t}(\boldsymbol{f}) \otimes U_i(-\lambda f_l \boldsymbol{f})]_{\boldsymbol{f}=\boldsymbol{\rho}_2/\lambda f_l} \tag{15}$$

where $\otimes$ denotes the operation of mathematical convolution. Thus, the output

field is the spatial convolution of the input field and the spatial content of the filter. This principle is used in the construction of optical correlators. Note that the 4-f system pictured in Figure 6 is symmetric. Suppose unequal focal length lenses were used, where we f_{l1} is the focal length of the lens in the $z=f_l$ plane and f_{l2} is the focal length of the lens in the $z=3f_l$ plane, Then the size of the image in the output plane $z=4f_l$ would scale with the respect to the image in the input plane $z=0$ as the ratio of the focal lengths f_{l2}/f_{l1}.

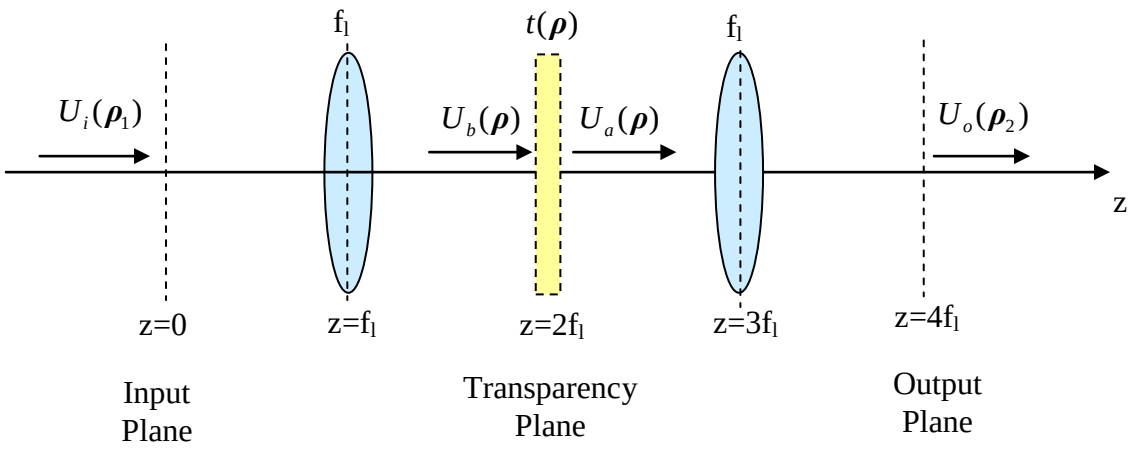

Figure 6. Symmetric 4-f imaging system. The presence of transparency in the $z=2f_l$ plane is optional.

3 Basics of Holography

3.1 Sinusoidal Holographic Grating

A simple sinusoidal holographic grating can be written by two monochromatic plane waves $E_1 = \hat{e}_1 A_1 e^{i(\omega t - \boldsymbol{k}_1 \cdot \boldsymbol{r})}$ and $E_2 = \hat{e}_2 A_2 e^{i(\omega t - \boldsymbol{k}_2 \cdot \boldsymbol{r})}$ interfering inside the photosensitive material. For simplicity, assume that A_1 and A_2 are real, and the waves have the same polarizations ($\hat{e}_1 \cdot \hat{e}_2 = 1$). The intensities of the two beams are $I_1 = |A_1|^2$ and $I_2 = |A_2|^2$. Intensity distribution of the interference pattern inside the material is given as

$$I \propto |E_1 + E_2|^2 = I_1 + I_2 + 2\sqrt{I_1 I_2}\cos(\boldsymbol{K}_G \cdot \boldsymbol{r}) = I_0[1 + m\cos(\boldsymbol{K}_G \cdot \boldsymbol{r})] \tag{16}$$

where

$$\boldsymbol{K} = \boldsymbol{k}_1 - \boldsymbol{k}_2 \tag{17}$$

is the grating vector, $I_0 = I_1 + I_2$, and

$$m = \frac{2\sqrt{I_1 I_2}}{I_1 + I_2} \tag{18}$$

is the grating modulation depth. The spatial pattern of the intensity profile creates a grating in the holographic material by modifying the index of refraction of the material, so that $n = n_0 + \Delta n$, where n_0 is the refractive index prior to illumination. The hologram (or holographic grating) is defined to be the spatial modulation of the refractive index of the material

$$\Delta n = n_1 \cos(\boldsymbol{K} \cdot \boldsymbol{r}) \tag{19}$$

where n_1 is the amplitude of the modulation, and the periodicity of the index modulation

$$\Lambda = 2\pi / K \tag{20}$$

also known as the grating wavelength, is the same as the periodicity of the light standing wave pattern. This grating can diffract light. The physical processes that give rise to the grating will be explained in the next chapter. The process of grating formation is sketched in Figure 7(a). In general, angles of incidence are not equal ($\theta_1 \neq \theta_2$), so that the grating is slanted at an angle ϕ. When the grating is illuminated with the plane wave in the direction of $\boldsymbol{k}_1$ ($\boldsymbol{k}_2$), the plane wave in the direction of $\boldsymbol{k}_2$ ($\boldsymbol{k}_1$) is reconstructed. Figure 7(b) shows reconstruction of the plane wave in the direction of $\boldsymbol{k}_2$.

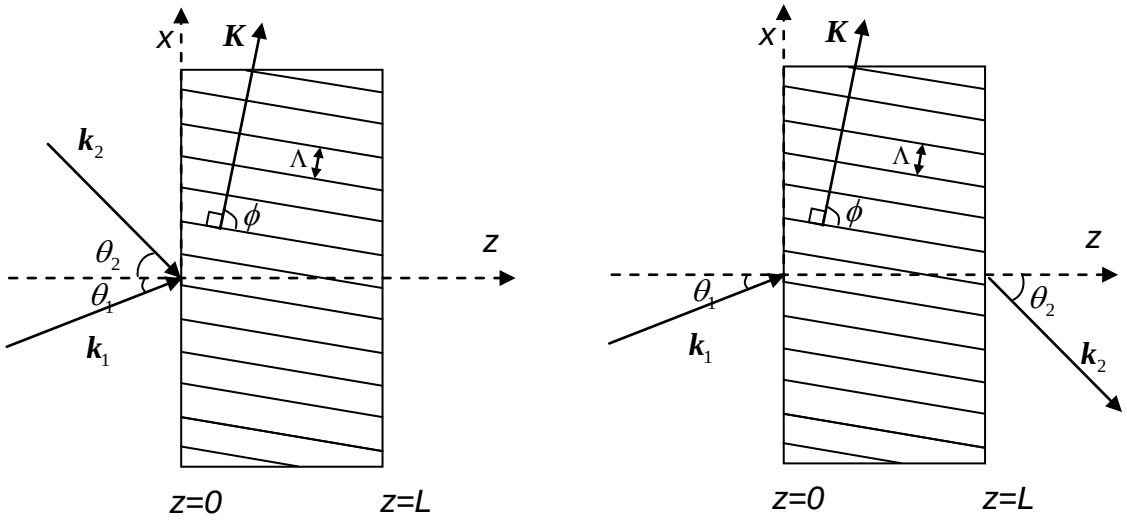

Figure 7. Holographic grating (a) formation and (b) readout

Sometimes the holographic grating is expressed as the modulation of the dielectric constant of the material

$$\varepsilon = \varepsilon_0 + \varepsilon_1 \cos(\boldsymbol{K}_G \cdot \boldsymbol{r}) \tag{21}$$

Note that typical values of n_1 for the diffraction problems of interest in this

thesis are on order of 10^{-3} to 10^{-4}, while $n_0 \approx 1.5$, so that the weak modulation condition $n_1 << n_0$ is usually valid. This allows us to relate the modulation of the refractive index to the modulation of the dielectric constant of the material via

$$\begin{aligned} n = \sqrt{\varepsilon} &= \left(\varepsilon_0 + \varepsilon_1 \cos(\boldsymbol{K}\cdot\boldsymbol{r})\right)^{1/2} = \\ &= \sqrt{\varepsilon_0} + \frac{\varepsilon_1}{2\sqrt{\varepsilon_0}}\cos(\boldsymbol{K}\cdot\boldsymbol{r}) = n_0 + n_1\cos(\boldsymbol{K}\cdot\boldsymbol{r}) \end{aligned} \tag{22}$$

where the first order Taylor series approximation was made because of the assumption that $\varepsilon_0 << \varepsilon_1$. Thus the average refractive index is $n_0 = \sqrt{\varepsilon_0}$, and the amplitude of the spatial modulation of the refractive index is $n_1 = \frac{\varepsilon_1}{2\sqrt{\varepsilon_0}}$.

3.2 Diffraction from Periodic Media

To gain more insight into diffraction process, we consider the scattering of a monochromatic plane wave from a periodic medium. Consider an extreme situation when the index modulation is lumped into an array of equidistant planes as depicted in Figure 8. In addition, we assume that these planes are infinite so that reflections from these planes are specular (i.e., mirror-like with angle of reflection equal to angle of incidence). Each of the planes reflects only a very small fraction of the incident plane wave. The scattered light consists of linear superposition of all these reflected plane waves. The diffracted beams are found when all these reflected plane waves add up constructively.

Let Λ be the spacing between these planes. This is also the period of the index variation. The path difference for rays reflected from two adjacent planes is $2\Lambda\sin\theta$,

where θ is the angle between the ray and the planes. Constructive interference occurs when the path difference is an integral number of wavelengths λ/n in the medium, so that

$$2\Lambda \sin\theta = N(\lambda/n) \tag{23}$$

where $n=n_0$ is the spatially averaged index of refraction of the medium and N is an integer. This is known as the Bragg law. Although reflection from each plane is specular, beam diffraction occurs only for certain values of θ_B which obey the Bragg law so that reflections from all planes add up in phase.

Equation (23) can also be written as

$$2k \sin\theta_B = NK \tag{24}$$

where k is the wave number of the light beam in the medium ($k = 2\pi m/\lambda$) and $K = 2\pi/\Lambda$ is the grating wave number. The left side of Equation (24), $2k\sin\theta_B$, is the change of the wave vector upon diffraction from the periodic medium. Thus the Bragg law can be interpreted as simply the conservation of momentum. Upon diffraction from a periodic medium (grating), the change of wave vector is exactly an integral number of the grating wave vector. Another way the Bragg law can be written is

$$\sin\theta_B = \frac{\lambda}{2n\Lambda} \tag{25}$$

Note that there are many Bragg angles, each corresponding to a different value of N.

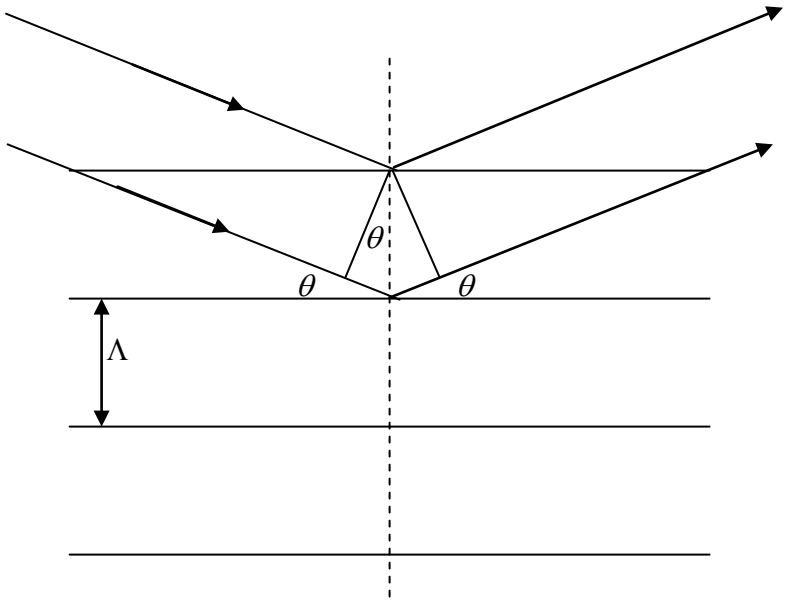

Figure 8. Scattering of monochromatic plane wave from a periodic medium

3.3 Criteria for Bragg and Raman-Nath Diffraction Regimes

If we decompose the periodic modulation of the index of refraction

$$n = n_0 + n_1 \cos(\boldsymbol{K} \cdot \boldsymbol{r}) \tag{26}$$

into its Fourier components, we obtain

$$n(r) = n_0 + n_1 \sum a_m e^{imKr} \tag{27}$$

where a_m is the *mth* Fourier component of the periodic index variation. We note that the *mth* Fourier component has a wave number of *mK*. Each of the Fourier components contributes to a diffraction order. In Bragg regime only the first order diffraction is allowed, whereas in Raman-Nath diffraction regime multiple diffraction orders can exist [18]. For the case sketched in Figure 8, Bragg diffraction is described by Equation

(24) with N=+1 or –1. It can be shown by rigorous analysis that the distinction between Bragg and Raman-Nath regimes depends on grating thickness and the magnitude of the refractive index modulation [19-21]. We will present the criteria for distinguishing the two diffraction regimes using qualitative arguments.

Consider the case of weak refractive index modulation (e.g. $n_1 < 10^{-3}$). Since the holographic material has a finite width, there is an uncertainty about the direction of the wave vector $\boldsymbol{K}$ of the recorded grating. However, conservation of energy dictates that the magnitude of $\boldsymbol{K}$ is finite. Multiple scattering will occur if the angular distribution of the grating wave vector $\boldsymbol{K}$ is large compared to the Bragg angle θ_B. Let L be the width of the grating. The angle of spreading of the grating wavevector ψ is determined from the uncertainty bandwidth product as $\Delta KL = 2\pi$, so that (see Figure 9)

$$\sin(\psi/2) = \Delta K / 2K \tag{28}$$

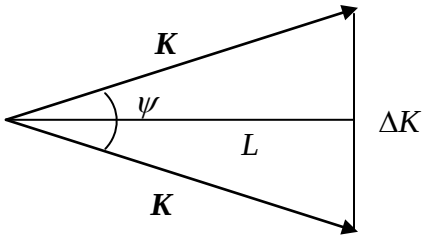

Figure 9. Angular spread of the grating wave vector

Assuming that $\Delta K << K$, we have $\psi \approx \Delta K / K$, so that

$$\psi \approx \frac{\Lambda}{L} \tag{29}$$

The Bragg angle is given approximately by (25)

$$\theta_B \approx \frac{\lambda}{2n_0\Lambda} \tag{30}$$

We now define a dimensionless parameter Q (also known as Klein and Cook parameter) [22]

$$Q \equiv 4\pi\theta_B / \psi \tag{31}$$

so that

$$Q = \frac{2\pi\lambda L}{n_0\Lambda^2} \tag{32}$$

It is customary to defines the regime of Q>10 as the Bragg regime of optical diffraction. Note that $Q \propto \frac{L}{\Lambda}$, so that a large Q means that the transverse length of the sample is much longer then the grating wavelength. In a thin grating, the transverse dimension of the periodic index variation is relatively small compared with the beam size and/or wavelength of light. When a plane wave is incident into the periodic medium, diffraction from each of the planes occurs in addition to specular reflection. The diffraction from each of these planes is a result of the finite size of the planes.

However, a large Q does not guarantee Bragg diffraction. It has been shown that for large refractive index modulation, gratings with Q > 10 produce multiple diffraction orders [23]. The amplitude of the refractive index modulation n_1 can be introduced through the parameter called the grating strength. The expression for the grating strength will be derived in Chapter 7 in the context of coupled-wave theory. In case of equal angle of incidence θ for both writing beams, the grating strength ν is

$$\nu = \pi n_1 L / \lambda \cos\theta$$

(33)

We define the dimensionless parameter ρ (also known as Raman-Nath parameter) [18]

$$\rho \equiv Q/(2\nu\cos\theta) \tag{34}$$

so that

$$\rho = \frac{\lambda^2}{\Lambda^2 n_0 n_1} \tag{35}$$

It is customary to define the regime where $\rho >> 1$ as the Bragg regime. Note that ρ is independent of the grating width *L*. Since $\rho \propto \frac{1}{n_1}$, it is clear that for weak modulation ρ is large, and conversely. Intuitively, the effect of the grating strength can be understood by noting that when modulation is large, we begin to approach the limiting case of Figure 7, so that multiple order diffraction is possible for thick gratings.

In summary, in order to determine which diffraction regime applies to a given problem, one has to consider both Q and ρ [24]. The validity of the Bragg diffraction regime requires that both Q>>1 and ρ >>1. The Ranan-Nath diffraction takes place when either Q<1 or ρ <1.

4 Four-Wave Mixing

4.1 Phase Conjugation by Degenerate Four-Wave Mixing

Phase conjugation optics in its most basic form deals with situations in which some input monochromatic optical field

$$E_1(\boldsymbol{r},t) = \mathrm{Re}[A(\boldsymbol{r})e^{i(\omega t-\boldsymbol{k}\cdot\boldsymbol{r})}] \tag{36}$$

is converted in real time to a new field that is proportional to

$$E_2(\boldsymbol{r},t) = \mathrm{Re}[A^*(\boldsymbol{r})e^{i(\omega t+\boldsymbol{k}\cdot\boldsymbol{r})}] \tag{37}$$

We note that E_2 can be obtained from E_1 by replacing the spatial part of the analytic function by its complex conjugate but leaving the factor $e^{i\omega t}$ as is. We refer to the field E_2 defined by (37) as the phase-conjugate replica of E_1 [25,26].

Consider the procedure of hologram recording and reconstruction as shown in Figure 10. In a photorefractive material recording and readout occur simultaneously, but for clarity we will consider each process separately. The first step (Figure 10(a)) shows the recording of a thin hologram using interference between a "reference" beam A_1 and a "signal" beam A_4. The resulting transmission function is

$$T \propto (A_4 + A_1)(A_4^* + A_1^*) = |A_4|^2 + |A_1|^2 + A_4A_1^* + A_1A_4^* \tag{38}$$

$A_1(\rho)$ and $A_4(\rho)$ denote the complex amplitudes of the reference and object fields, respectively, in the hologram plane $z=0$.

In the reconstruction step, the hologram is illuminated by a single reference wave A_2 impinging from the right in a direction opposite to that of A_1, as shown in Figure 10(b). We thus have $A_2 = A_1^*$, so that the diffracted field to the left of the hologram is

$$A_3 = TA_2 \propto (|A_4|^2 + |A_1|^2)A_1^* + (A_1^*)^2 A_4 + |A_1|^2 A_4^* \tag{39}$$

The first term on the right side of (39) is proportional to the incident field $A_2 (= A_1^*)$ and is of no interest. The term $(A_1^*)^2 A_4$ will, in a volume hologram, have a phase factor $e^{-i((2\boldsymbol{k}_1 - \boldsymbol{k}_4)\cdot r}$ and is thus phase mismatched, i.e., will not radiate. The term of interest is

$$A_3 \propto |A_1|^2 A_4^* = |A_1 A_2| A_4^* \tag{40}$$

which at z<0 corresponds to a "time reversed" phase conjugate replica of the original object field.

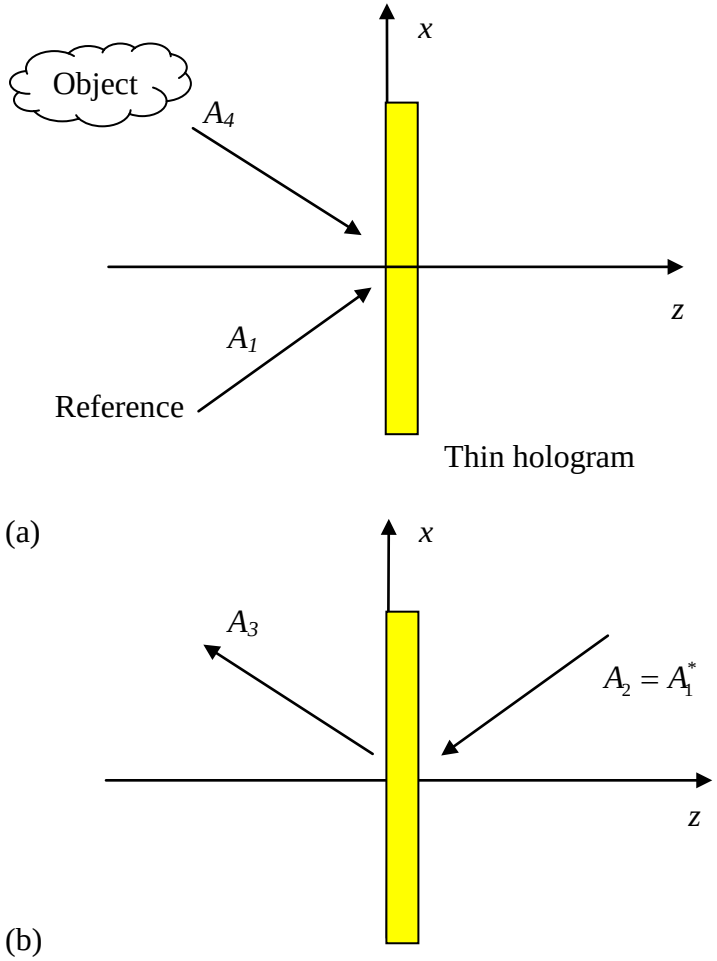

Figure 10. (a) Hologram recording (b) Reconstructing a phase conjugate $A_3 \propto A_4^*$

Consider next the four-wave mixing geometry of Figure 11. The nonlinear medium is characterized by a third order susceptibility $\chi^{(3)}$ which relates the induced polarization to the incident fields according to [27]

$$P^{(NL)}(\omega_4 = \omega_1 + \omega_2 - \omega_3) = \frac{1}{2}\chi^{(3)} A_1 A_2 A_3^* e^{i[\omega_4 t - (k_1 + k_2 - k_3)\cdot r]} \tag{41}$$

$$P^{(NL)}(\omega_3 = \omega_1 + \omega_2 - \omega_4) = \frac{1}{2}\chi^{(3)} A_1 A_2 A_4^* e^{i[\omega_3 t - (k_1 + k_2 - k_4)\cdot r]} \tag{42}$$

where A_j is the complex amplitude of the optical field, i.e.,

$$E_j(r,t) = \frac{1}{2} A_j(r) e^{i(\omega_j t - k_j \cdot r)} + c.c. \tag{43}$$

If the medium is illuminated by two intense pump waves A_1 and A_2 with $\omega_1 = \omega_2 \equiv \omega$ which travel in exact opposite to each other ($k_1 = -k_2$), and by a third weak object wave A_4 with $\omega_4 = \omega$, a reflected wave A_3 at ω is produced which is the complex conjugate ("time reversed") of A_4.

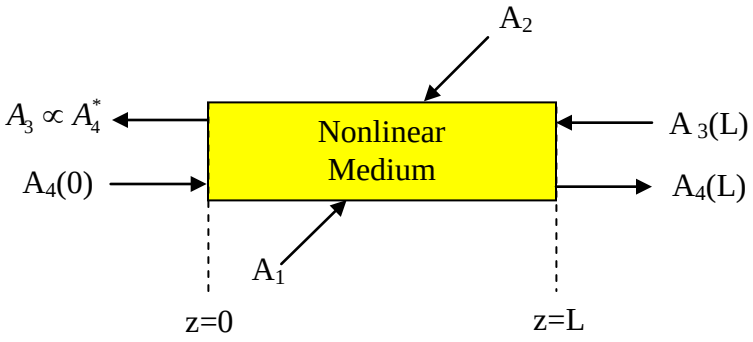

Figure 11. Geometry for four-wave mixing

This polarization can be viewed as a distributed source that radiates optical

waves at frequency ω, provided phase matching condition is satisfied. Thus we obtain [11,28]

$$A_3(z<0) = -i\left(\frac{\kappa^*}{|\kappa|}\tan(|\kappa| L)\right)A_4^*(z<0) \tag{44}$$

where

$$\kappa = \frac{\pi}{\lambda n_0}\chi^{(3)}A_1A_2 \tag{45}$$

Comparing (44) to (40) it is clear that formally, the nonlinear mixing of Figures 10 and 11 are equivalent. The analogy can be appreciated more fully if we write (44) in the limit of $|\kappa| L << 1$. In this case

$$A_3(z<0) \propto |A_1A_2|A_4^*(z<0) \tag{46}$$

which form is identical to (40). As a matter of fact, if we overlay Figures 10(a) and 10(b), the resulting figure is equivalent to Figure 11. This establishes the formal analogy between the two operations and hence the real-time holographic nature of four-wave mixing [29-32]. It should be emphasized that the two processes represent different physical phenomena and that the analogy is only operational. In four-wave mixing, the recording and the readout happen simultaneously. Phase conjugation by optical four-wave mixing is thus often referred to as real-time holography.

4.2 Real-Time Optical Correlators

4.2.1 Optical Correlation Theorem

The nonlinear optical process involved in a real-time optical correlator is four-wave mixing. There are four beams, i.e., three input beams (two images and a reference plane wave) and one output beam (correlation signal). Figure 12 shows the functional block diagram of the optical correlator based on the correlation theorem

$$A_1 * A_2 = \mathcal{F}^{-1}[\mathcal{F}(A_1)\mathcal{F}^{*}(A_2)] \tag{47}$$

where A_1 and A_2 represent two-dimensional images, $\mathcal{F}$ is the two-dimensional Fourier transform, and [16]

$$A_1 * A_2 = \int A_1(\boldsymbol{\rho}')A_2^{*}(\boldsymbol{\rho}' - \boldsymbol{\rho})d\boldsymbol{\rho}' \tag{48}$$

The significance of Equation (47) is that it contains only the Fourier transforms of A_1 and A_2 that can be easily implemented optically by using lenses, while Equation (48) contains a double integral that is not an explicit form that can be implemented optically. Moreover the time needed for a Fourier-transform operation is as short as the time needed for light to travel less than twice the focal length of the lens, which is usually only a few nanoseconds. The multiplication operation on the right side of Equation (47) can be implemented by holographic real-time writing and reading. In this case, the result of the multiplication $\mathcal{F}(A_1)\mathcal{F}^{*}(A_2)$ is proportional to the intensity of the diffracted beam. The inverse Fourier transform of $\mathcal{F}(A_1)\mathcal{F}^{*}(A_2)$ can be again performed by a lens.

In general, in a correlation-theorem-based optical correlator, there are two possible configurations, as shown in Figure (2): the VanderLugt (VLC) configuration and the joint tranform configuration (JTC). In the VLC configuration, the hologram is written by the Fourier transform of one image, say, the input scene, and a reference beam, usually a plane wave, and read out by the Fourier transform of the reference image. In the JTC configuration, the hologram is written by the Fourier transforms of the input scene and the reference image, and read by a plane wave.

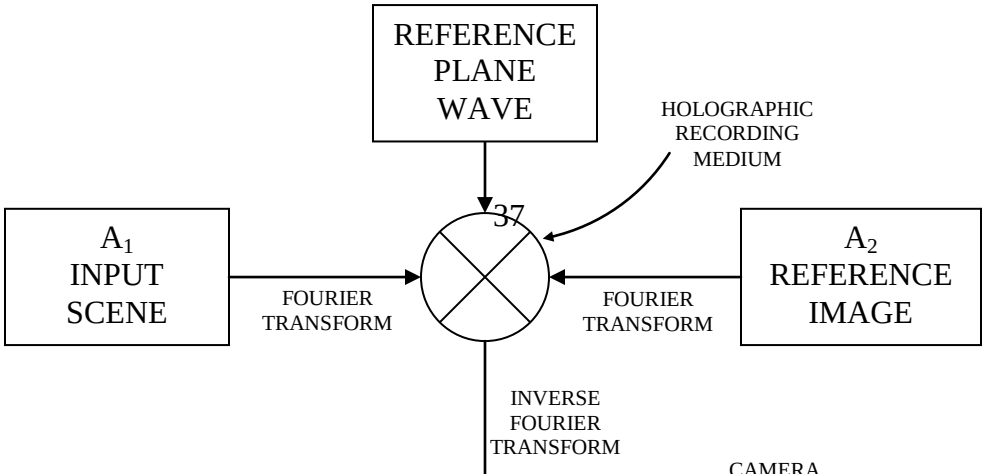

Figure 12. Block diagram of a correlation-theorem-based optical correlator system.

4.2.2 Real-time VanderLugt Correlator

Figure 13 presents the basics of a real-time VLC [12]. A_1 and A_2 are paraxial monochromatic beams bearing the input scene image and a reference image, respectively, and R is a reference plane wave. The grating in the dynamic material is written by R and $\tilde{A}_1$, the spatial Fourier transform of A_1. From the discussion in the section 4.1, the transmission function of the hologram is

$$T \propto |\tilde{A}_1 + R|^2 = |\tilde{A}_1|^2 + |R|^2 + \tilde{A}_1^* R + \tilde{A}_1 R^* \tag{49}$$

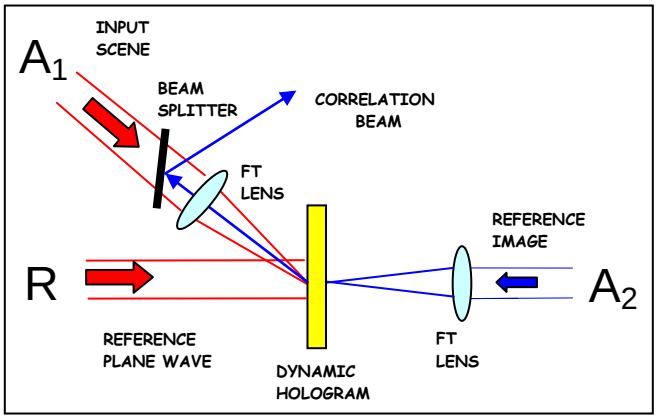

Figure 13. Real-time VanderLugt correlator implemented in a FWM setup

The beam bearing the *FT* of the filter image $\tilde{A}_2$, which is usually incoherent with the two writing beams, is incident on the hologram exactly counter-propagating to the reference beam *R*. After the hologram we have four terms

$$(|\tilde{A}_1|^2 + |R|^2)\tilde{A}_2 + \tilde{A}_1^* R\tilde{A}_2 + \tilde{A}_1 R^* \tilde{A}_2 . \tag{50}$$

Due to phase matching, the term $\tilde{A}_1^* R\tilde{A}_2$ is producing a phase-conjugated beam of $\tilde{A}_1$. After the phase- conjugated beam passes through the Inverse Fourier-transforming (IFT) lens, one obtains $\mathcal{F}\{\tilde{A}_1^* \tilde{A}_2 R\}$ which gives $A_1 * A_2$. Note that *R* has constant amplitude which factors out during the IFT operation, and a phase factor, which only shifts the variable of the correlation function. Therefore, *R* has no impact on the correlation functional form, which is why a plane wave was chosen to be a reference wave in first place.

4.2.3 Real-time Joint-Transform Correlator

The real-time JTC architecture [33], which is very similar to the VLC architecture, is shown in Figure 14. In the JTC architecture, the Fourier transforms of the input scene and reference images, i.e., $\tilde{A}_1$ and $\tilde{A}_2$ are recorded in the dynamic holographic medium. Thus, the transmission function of the grating formed is given by

$$T \propto |\tilde{A}_1 + \tilde{A}_2|^2 = |\tilde{A}_1|^2 + |\tilde{A}_2|^2 + \tilde{A}_1^* \tilde{A}_2 + \tilde{A}_1 \tilde{A}_2^* \tag{51}$$

The read beam, which is incoherent with the writing beams, is the plane wave *R* that is

counter-propagating to the beam $\tilde{A}_2$. After the readout we have

$$(|\tilde{A}_1|^2 + |\tilde{A}_2|^2)R + \tilde{A}_1^* \tilde{A}_2 R + \tilde{A}_1 \tilde{A}_2^* R \tag{52}$$

Again, the term $\tilde{A}_1^* \tilde{A}_2 R$ gives rise to a phase-conjugated beam $\tilde{A}_1^*$, and after the Fourier transforming lens one obtains $A_1 * A_2$.

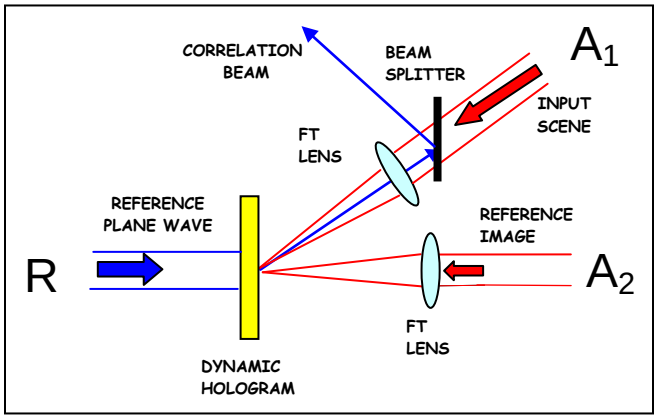

Figure 14. Real-time Joint Transform Correlator implemented by FWM

4.2.4 Efficiency of Operation

Mathematically these two configurations are similar, but in real-time implementations there is a difference in the system speed limitations. In the VLC configuration the image in the read beam may be changed faster than the speed allowed by the holographic medium because the read beam is not responsible for creating the hologram [34]. On the contrary, in the JTC method none of the image beams can be changed faster than the speed allowed by the holographic medium because they are the writing beams. Note that both JTC and VLC are automatically shift invariant correlators by the virtue of shift-invariance property of the Fourier transform. However, an issue that occurs in a volume holographic medium-based correlator is the incidence angle limitation imposed by the Bragg diffraction process.

5 Photorefractive Effect in Polymers

5.1 Advantages of Photorefractive Polymers

The photorefractive (PR) effect refers to spatial modulation of the index of refraction generated by a specific mechanism: light induced charge redistribution in a material in which the index of refraction depends upon the electric field [35,36]. The photorefractive effect was first identified in the electro-optic crystal $LiNbO_3$ where its consequence was first reported as a reversible form of optical damage to the transmission of an incident beam through the crystal. Since then, the photorefractive effect has been onserved in a number of inorganic crystals, such as $KNbO_3$, $BaTiO_3$ (BTO), $Bi_{12}SiO_{20}$ (BSO), $Sr_xBa_{1-x}NbO_3$ (SBN), InP:Fe. All photorefractive inorganic materials are electro-optic crystals doped with donor and acceptor impurities. The photorefractive effect arises when charge carriers, photogenerated from the impurities by a spatially modulated light intensity, separate by drift and diffusion processes and become trapped to produce a non-uniform space-charge distribution. The resulting internal space-charge electric field then modulates the refractive index of the material via the linear electro-optic effect (Pockel's effect) to create a phase grating or hologram that can diffract a light beam.

Holography using photorefractives has been proposed as a useful process with many potential applications, and there have now been two decades of diverse optical research that has explored these. One of the reasons photorefractive crystals have not realized commercial success is that the ferroelectric crystals that exhibit the effect are costly to grow, cut and polish. The photorefractive effect is based on the impurity content in the crystals and this is difficult to control through a crystal boule as it is grown. For this reason, reproducibility of results can be difficult to attain when comparing different crystals in different situations. For these reasons, there was strong interest to develop polymer composites that show the photorefractive effect. A polymer can be injection molded, spin coated into optical waveguide films, embossed into channels, and end facets can be produced with a quality-dicing saw. There is no need for the costly crystal growth process or for polishing processes when a polymer can be used.

5.2 Photorefractive Polymer Compostite Structure

A typical photorefractive polymer consists of four different organic materials mixed together to form a composite [37]. The polymer matrix is poly(N-vinylcarbazole), PVK, a well-known hole transport matrix. PVK becomes a photoconductor in visible light when a small amount of 2,4,7-trinitro-9-fluoreno (TNF) is added. The photoexcitation of PVK-TNF leads to electron transfer from a side group of the PVK matrix onto a stationary TNF molecule that becomes a (negatively charged) anion. A mobile electron vacancy (a hole) is left behind on the matrix. Either diffusion or, more importantly, drift in an applied field will move the hole through the matrix, and as it moves, the positive charge associated with it is attracted to other TNF anions fixed at various locations in the matrix. If the hole is captured by an anion then the two

charges combine to produce a neutral TNF molecule as the hole is annihilated. The other two constituents of the photorefractive composite are the electro-optic dye and an additive that makes the material more plastic. The shear viscosity of the individual dye molecules is reduced in the plastic environment to the point where dye molecules can rotate to respond to local changes in the static electric field.

5.3 Physics of Photorefraction in Amorphous Polymers

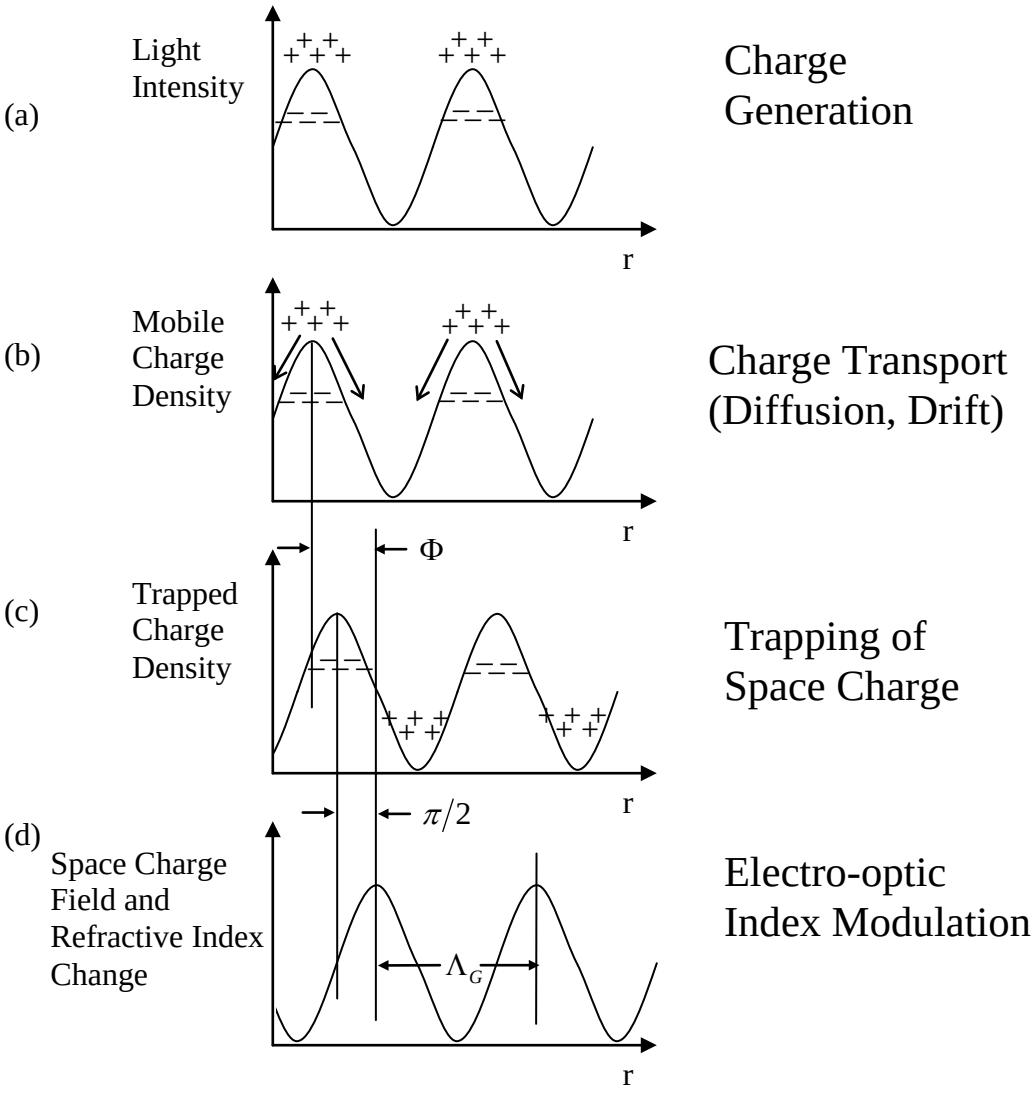

Figure 15. Photorefractive Effect in Polymers

In Figure 15 we review the miscroscopic processes required to produce a hologram by the PR mechanism [38,39]. Figure 15(a) shows the optical standing wave pattern of intensity that is produced by two intersecting coherent beams of light. This time-independent but spatially modulated intensity pattern consists of light and dark planes throughout the intersection region, which has a spatial wavelength of periodicity Λ_G, which can be shown to be equal to

$$\Lambda_G = \frac{\lambda_0}{2n_0 \sin[(\theta_2 - \theta_1)/2]} \tag{53}$$

Where n_0 is the index of refraction of the material, λ_0 is the optical wavelength in free space, and θ_1 and θ_2 are the internal angles of incidence of the two writing beams relative to the sample normal. For easily accessible opening angles between the two light beams and optical wavelengths, the grating wavelength is in the range 0.3-20μm. The direction normal to the light and dark planes is taken as the direction of the grating wavevector $\boldsymbol{K}_G$, the magnitude of which is given by the usual formula $K_G = 2\pi/\Lambda_G$. If $\boldsymbol{r}$ is the direction of the grating wavevector, the optical intensity follows the offset sinusoidal pattern shown in Figure 15(a).

The first physical process required for the PR effect is the generation of mobile charge in response to the spatially varying illumination. This may be viewed as the separation of electrons and holes induced by the absorption of the optical radiation, denoted as plus and minus charges in the figure. In organic materials, this effect is likely to be strongly field dependent.

The second element for the PR effect is the transport of the generated charges, with one carrier being more mobile than the other. In Figure 15(b), the holes are shown to be more mobile, which is the more common case for organics. (If both carriers are equally mobile, the resulting space-charge distribution could have zero internal electric field and hence no PR effect.) The physical processes giving rise to charge transport are either diffusion due to density gradients or drift in an externally applied electric field. Since most polymeric materials with sufficient optical transparency are

relatively good insulators, the ability of generated charges to move by diffusion alone is quite limited. In essentially all of the cases, drift is the dominant mechanism for charge transport that stimulates charge to hop from transport molecule to transport molecule.

The third element for the PR effect, especially when long grating lifetimes are desired, is the presence of trapping sites that hold the mobile charge. In real materials, the exact identity of the trapping sites is seldom known in detail. In general terms, a trapping site is a local region of the material where the mobile charge is prevented from participating in transport for some period of time. For example, in the hopping picture, a site with lower total energy for the charge may act as a trap, and lifetime of the carrier in the trap will be determined by the trap depth compared to thermal energies.

After separation of charge carriers occurs, the resulting space charge density is shown in Figure 15(c). Via Poisson's equation of electrostatics such a charge distribution produces a sinusoidal space-charge electric field as shown in figure 1d. Since Poisson's equation relates the spatial gradient of the electric field to the charge distribution, the resulting internal electric field is shifted in space by 90^o relative to the trap charge, or one quarter of the grating wavelength.

Finally, if the optical index of refraction of the material changes in response to an electric field, a spatial modulation of the index of refraction results as shown in figure 1d. Foe example, if the material has a linear electrooptic effect (which is a $\chi^{(2)}$ process), the magnitude of the index modulation Δn is related to the magnitude of the space-charge field E_{sc} by the relation [27]

$$\Delta n = -(1/2)n^3 r_e E_{sc} \tag{54}$$

where r_e is the effective electrooptic coefficient for the geometry under consideration. A sinusoidally varying index modulation is a grading that can diffract light.

The total spatial phase shift between the peaks of the optical intensity pattern in figure 15(a) and the peaks of the index of refraction modulation in figure 15(d) is denoted Φ. As an external electric field is applied and drift and diffusion compete, Φ can depart from $\pi/2$, but at sufficiently high fields, where the drift mechanism for photoconduction is dominant, Φ again approaches $\pi/2$. Thus, in organics where high fields are generally

required and diffusion is weak or absent, Φ approaches the π/2 value.

5.4 Orientational Enhancement Effect

The entire sample must be made noncentrosymmetric by using an applied field, also called the poling field or bias field to achieve net orientation of all the chromophores by the interaction between the dipole moment of the NLO molecules and the applied field. The poling may result in quasi-permanent orientation, but in most PR polymers the external field must be continuously applied to the sample. A modified refractive index is obtained in poled polymer devices through the creation of asymmetry in the polarizability of an electro-optic dye distribution. A polar dye molecule has a positively charged region and a separate region of negative charge and a steady applied field can orient the relative positions of these charge regions, although the molecule remains fixed in space. Any additional changes in electric field will lead to polarization that depends on the direction of the new field. A new contributing term to the polarization appears which is dependent on the square of the electric field and this leads to the Pockel's electro-optic shift in the refractive index. A more significant change in the refractive index is observed through the anisotropy of the dye molecules, which is know as the orientational enhancement effect [40]. Dye molecules can rotate to respond to local changes in the static electric field. There will be more alignment of the dye molecules as the applied field becomes stronger relative to the randomizing effect of Brownian motion at room temperature. The simplest description of the anisotropy of the refractive index of the molecules is that the index is given by

$$n = n_0 + \Delta n \cos^2 \psi$$

(55)

where n_0 is the smallest value, and ψ is the angel between the dominant molecular axis and the probing optical electric field. The mean value of $\cos^2\psi$ is to a good approximation proportional to the poling field squared. Molecular reorientation therefore leads to a change in refractive index that is proportional to E^2, mimicking the Pockel's electro-optic effect. Each dye molecule is itself highly anisotropic such that the polarizability is much higher along the molecular axis than it is for electric fields across the molecular axis. In this case, turning the molecule toward the electric field of a light wave increases the refractive index experienced by that wave, as shown in Figure 16. The effect on refractive index of the local reorientation of the anisotropic polarizability profiles of the dye molecules due to a patterned electric field can be an order of magnitude greater than the effect of the Pockel's electro-optic nonliniarity in a typical photorefractive composite. For this reason, plasticized amorphous compounds exhibit far stronger optical diffraction in photorefraction than do comparable materials without such freedom to reorient at the molecular level.

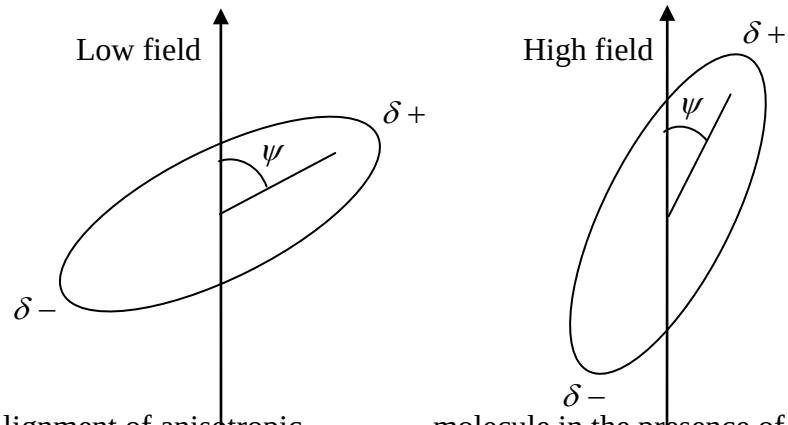

Figure 16. Alignment of anisotropic molecule in the presence of electric field

5.5 Rate Equation Model of Photorefraction in Polymers

The original rate equation theory of Kukhtarev [7,8] was intended to describe the generation of space-charge field due to non-uniform illumination of an inorganic photorefractive material. The approach utilized a standard current equation, a continuity equation (for a single mobile charged species), Poisson's equation to relate the internal field to the charge density, and the rate equation for the single charged species. Here we present this model modified to account for the physical processes that occur in polymeric photorefractives. The relevant photogeneration process active in the illumination regions may be desribed by [38]

$$G + h\nu \rightarrow G^{-} + hole \tag{56}$$

where *G* designates the generator molecule. The trapping can be described by

$$Tr + hole \rightarrow Tr^{+} \tag{57}$$

were *Tr* designates an unoccupied trapping site. Assuming two-body recombination and thermally activated detrapping, rate equations for the traps and the generators are given by

$$\frac{\partial N_G^-}{\partial t} = \frac{s\phi I}{h\nu} N_G - \gamma_R p N_G^- \tag{58}$$

$$\frac{\partial N_T^+}{\partial t} = \gamma_T p N_T - N_T^+ \nu_0 e^{-\Delta_T / kT} \tag{59}$$

with p = hole density, N_G = generator density, N_G^- = density of reduced generators, N_T = (unoccupied) trap density, N_T^+ =density of occupied traps, , γ_T = two body trapping coefficient, γ_R = two-body recombination coefficient, I = irradiance, T = temperature, s = absorption cross section, e = electron charge, $\phi(E)$ = quantum efficiency, and ν_0, Δ_T = thermal detrapping parameters. Thus, the full continuity equation is

$$\frac{\partial p}{\partial t} = -\frac{1}{e}\nabla \cdot j + \frac{s\phi I}{h\nu} N_G - (\gamma_T N_T + \gamma_R N_G^-) p - N_T^+ \nu_0 e^{-\Delta_T / kT} \tag{60}$$

where j = current density. The expression for the current density due to drift and

diffusion is

$$j = e\mu p(E_0 + E_{sc}) + eD\nabla p \tag{61}$$

with $\mu(E)$ = mobility and D = diffusion coefficient. Poisson's equation provides the crucial link between the total internal field and the space-charge density

$$\nabla \cdot (E_0 + E_{sc}) = \frac{e}{\varepsilon_r \varepsilon_0}(p + N_T^+ - N_G^-) \tag{62}$$

The conservation of sites is expressed by

$$N_G^o = N_G + N_G^- \tag{63}$$

$$N_T^o = N_T + N_T^+ \tag{64}$$

These equations must be solved with the assumed optical intensity pattern

$$I = I_0(1 + m\cos(K_G \cdot r)) \tag{65}$$

where m is the contrast of the interference pattern. Specific models must be assumed for the field dependence of ϕ, μ, and the recombination rate constants in order to complete the physical model. It is clear that this set of equations cannot be solved exactly. Two approaches are available: numerical solution and linearization to develop analytical solutions of the zero-order and first order Fourier components of the space-charge field [41]. Assuming the condition that once a charge is trapped, it cannot be released (deep trap), a steady state expression for the first-order Fourier component of the space-charge field was obtained in the limit of high trap density and small photogeneration relative to trapping [42]. For reference, we recall that the steady state space-charge field in the standard one-carrier PR model used for inorganic materials is [43,44]

$$E_{sc} = \frac{mE_0(E_0 + iE_d)}{E_q + E_d - iE_0} \tag{66}$$

where $E_q = eN_A(1 - N_A / N_D)/(\varepsilon_0 \varepsilon_r K_G)$ is the trap-density limited space-charge field, N_D is the density of donors, and N_A is the density of acceptors, and $E_d = k_B T K_G / e$ is the diffusion field. The corresponding expression for organic PR materials is quite similar, with the density of donors replaced by the density of traps, and with additional field-dependent terms arising from the field dependence of mobility and quantum efficiency.

5.6 Connection to Optical Signal Processing

The main result of these calculations for the use in optical signal processing is that we can express the refractive index modulation as

$$n = n_0 + \Delta n \tag{67}$$

where

$$\Delta n = n_1 \cos(\boldsymbol{K}_G \cdot \boldsymbol{r}) \tag{68}$$

where n_1 is the amplitude of the refractive index modulation. One can see that n_1 depends on the external field E_0, the orientation of the sample, and the modulation depth *m*. The last condition has implications that by adjusting writing beam ratios, one can modulate the grating diffraction efficiency, since

$$m = 2\sqrt{I_1 I_2}\,/\,(I_1 + I_2) = 2\sqrt{\beta}\,/\,(1+\beta) \tag{69}$$

where $\beta = I_1 / I_2$ is the ratio of the intensities. If the beam envelopes are not spatially uniform, diffraction can be effectively suppressed in the spatial region of the hologram

where $\beta << 1$. This technique can be used for real-time edge enhancement, as will be discussed in later sections [45].

5.7 Four-Wave Mixing in Photorefractive Polymers

Figure 17 shows the typical experimental geometry for the four-wave mixing (FWM) PR grating measurements. The bias electric field $\boldsymbol{E}_0$ is applied to the transparent electrodes of indium-tin-oxide (ITO) coated on glass, between which a layer of varying thickness of 10 to 100μm of the PR polymer composite is sandwiched. The gratings are written by beams 1 and 2, which enter the sample with angles θ_1 and θ_2 (all angles are defined with respect to the sample normal inside the material). The two writing beams are mutually coherent and have the same polarization. The grating is written at a wave vector $\boldsymbol{K}_G$, with an angle θ_G to the external electric field $\boldsymbol{E}_0$. For the FWM experiments, the grating is probed with beam 3, which is collinear and counter propagating to beam 2. The diffracted beam appears collinear and counter propagating to beam 1. In probing the grating, it is important that beam 3 does not affect the grating or does not interact with writing beams. This can assured by making the probe beam much weaker than the pump beams and by having the probe beam polarized orthogonal to the writing beams. Because the NLO chromophores are normally aligned in the direction of the poling field, the normal of the sample must be rotated with respect to the bisector of the writing beams to provide a nonzero r_e along the grating vector $\boldsymbol{K}_G$. In addition, this oblique geometry provides a non-zero component of the externally applied dc field along $\boldsymbol{K}_G$ to enable

drift of the photogenerated charge carriers in the direction of $\boldsymbol{K}_G$. For these reasons, the oblique geometry is usually the geometry of choice, with typical values of the external inter-beam angle $\theta_{ext} = 30^o$, and the sample tilt angle $\Psi_{ext} = 45^o$. The diffraction efficiency of the material is defined as the ratio of the diffracted power to the incident beam power, $\eta = I_4 / I_3$ (for equal spot sizes).

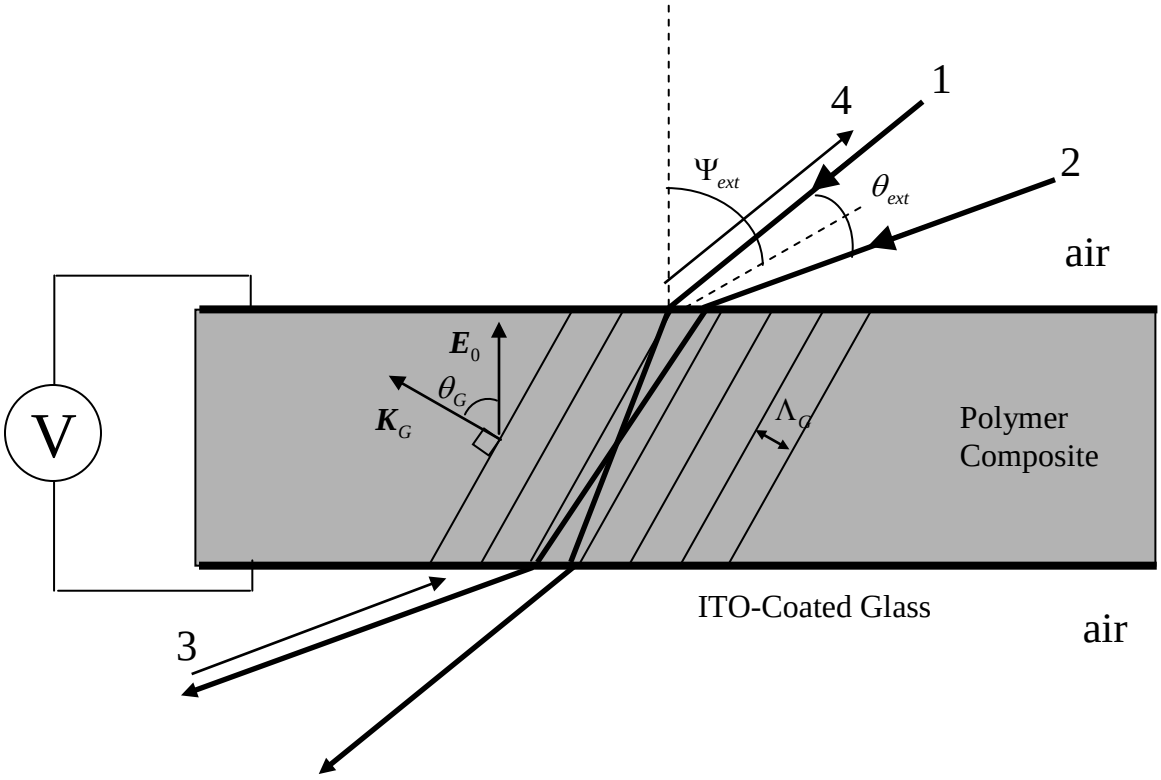

Figure 17. Four-wave mixing in a photorefractive polymer

6 Volume Diffraction in the Born Approximation

6.1 Scattering from Volume Gratings

In most holographic materials, volume holograms are recorded as modulation of the material refractive index, resulting after exposure to the interference pattern between the signal and reference beams. Consider such as dielectric material, occupying volume V in space, with position- dependent dielectric constant $\varepsilon(\boldsymbol{r})$. We assume that modulation is weak and narrowband, i.e.

$$\varepsilon(\boldsymbol{r}) = \varepsilon_0 + \tilde{\varepsilon}(\boldsymbol{r})e^{i\boldsymbol{K}_g\cdot\boldsymbol{r}}, \qquad \varepsilon_0 >> \left|\tilde{\varepsilon}(\boldsymbol{r})\right| \tag{70}$$

Here ε_0 is the dielectric constant before exposure, $\boldsymbol{K}_g$ is the carrier wave-vector of the grating, and $\tilde{\varepsilon}(\boldsymbol{r})$ is a low-bandwidth modulation (in the sense that the maximum spatial frequency contained in $\tilde{\varepsilon}(\boldsymbol{r})$ is much less than $\boldsymbol{K}_g$) representing the data stored in the volume hologram. The hologram is illuminated with an incident optical field $\boldsymbol{E}_p$ at frequency ω. In this section, we derive the diffracted field $\boldsymbol{E}_d$, under some approximations, as the first-order solution to a wave scattering problem [46,47]. The result is the diffraction integral (84).

The time-harmonic electromagnetic field satisfies Maxwell's equations in charge-free space:

$$\begin{aligned} \nabla\times\boldsymbol{E} &= i\omega\boldsymbol{B} & \nabla\cdot\boldsymbol{D} &= 0 \\ \nabla\times\boldsymbol{H} &= -i\omega\boldsymbol{D} & \nabla\cdot\boldsymbol{B} &= 0 \end{aligned} \tag{71}$$

where $\boldsymbol{E} = \boldsymbol{E}_p + \boldsymbol{E}_d$ is the total electric field, $\boldsymbol{D} = \varepsilon\boldsymbol{E}$ is the dielectric displacement, $\boldsymbol{H}$ is the magnetic field, $\boldsymbol{B} = \mu\boldsymbol{H}$ is the magnetic induction, and μ is the magnetic

permeability. Because we are dealing with a dielectric non-magnetic materials, $\mu = \mu_0$, the magnetic permeability in vacuum. From the curl equations,

$$\nabla \times \nabla \times \boldsymbol{E} = -\mu_0 \varepsilon(-\omega^2 \boldsymbol{E}) \tag{72}$$

hence

$$\nabla(\nabla \cdot \boldsymbol{E}) - \nabla^2 \boldsymbol{E} = \omega^2 \mu_0 \varepsilon \boldsymbol{E} \tag{73}$$

To calculate $\nabla \cdot \boldsymbol{E}$, we use Gauss's law:

$$\nabla \cdot (\varepsilon \boldsymbol{E}) = \nabla \varepsilon \cdot \boldsymbol{E} + \varepsilon \nabla \cdot \boldsymbol{E} = 0, \tag{74}$$

hence

$$\nabla \cdot \boldsymbol{E} = -\frac{\nabla \varepsilon \cdot \boldsymbol{E}}{\varepsilon} \approx -\frac{\nabla \varepsilon \cdot \boldsymbol{E}}{\varepsilon_0} \tag{75}$$

The modulation gradient is calculated explicitly as

$$\nabla \varepsilon(\boldsymbol{r}) = \nabla\left(\tilde{\varepsilon}(\boldsymbol{r}) e^{i\boldsymbol{K}_g \cdot \boldsymbol{r}}\right) = e^{i\boldsymbol{K}_g \cdot \boldsymbol{r}} \nabla \varepsilon(\boldsymbol{r}) + i\tilde{\varepsilon}(\boldsymbol{r}) \boldsymbol{K}_g e^{i\boldsymbol{K}_g \cdot \boldsymbol{r}} \tag{76}$$

The narrow-band grating assumption implies that the first term is negligible, and thus we obtain

$$\frac{\nabla \varepsilon \cdot \boldsymbol{E}}{\varepsilon_0} = -i \frac{(\boldsymbol{K}_g \cdot \boldsymbol{E}) \tilde{\varepsilon}(\boldsymbol{r}) e^{i\boldsymbol{K}_g \cdot \boldsymbol{r}}}{\varepsilon_0} \tag{77}$$

The wave equation for the electric field in the presence of volume gratings takes form

$$\nabla^2 \boldsymbol{E} + \omega^2 \mu_0 \varepsilon_0 \boldsymbol{E} = -i\nabla\left(\frac{(\boldsymbol{K}_g \cdot \boldsymbol{E}) \tilde{\varepsilon}(\boldsymbol{r}) e^{i\boldsymbol{K}_g \cdot \boldsymbol{r}}}{\varepsilon_0}\right) - \omega^2 \mu_0 \tilde{\varepsilon}(\boldsymbol{r}) e^{i\boldsymbol{K}_g \cdot \boldsymbol{r}} \boldsymbol{E} \tag{78}$$

Using the narrow-band approximation, the first term on the right hand side simplifies to

$$\approx -i\left[(\boldsymbol{K}_g \nabla)\boldsymbol{E} + i(\boldsymbol{K}_g \cdot \boldsymbol{E})\boldsymbol{K}_g\right] \tilde{\varepsilon}(\boldsymbol{r}) e^{i\boldsymbol{K}_g \cdot \boldsymbol{r}} / \varepsilon_0 \tag{79}$$

we denote by $\boldsymbol{K}_g\nabla$ the outer product of the two operators. We now define the matrix operator

$$\begin{aligned} U(\boldsymbol{r}) &= \tilde{\varepsilon}(\boldsymbol{r})e^{i\boldsymbol{K}_g\cdot\boldsymbol{r}}\left[\frac{-i(\boldsymbol{K}_g\nabla)+\boldsymbol{K}_g(\boldsymbol{K}_g\cdot)}{\varepsilon_0}+\omega^2\mu_0\right]= \\ &= \frac{\tilde{\varepsilon}(\boldsymbol{r})}{\varepsilon_0}e^{i\boldsymbol{K}_g\cdot\boldsymbol{r}}\left[-i(\boldsymbol{K}_g\nabla)+\boldsymbol{K}_g(\boldsymbol{K}_g\cdot)+k^2\right] \end{aligned} \tag{80}$$

where we used $k = 2\pi/\lambda = \omega\sqrt{\mu_0\varepsilon_0}$. The wave equation takes the compact form

$$\left(\nabla^2+k^2\right)\boldsymbol{E} = U(\boldsymbol{r})\boldsymbol{E} \tag{81}$$

The volume diffraction problem is formally equivalent to scattering of the vector field $\boldsymbol{E}$ from the potential $U(\boldsymbol{r})$. Let $G(\boldsymbol{r})$ denote Green's matrix for the inhomogeneous wave equation corresponding to (81). The solution is a series of diffracted orders

$$\boldsymbol{E} = \boldsymbol{E}_p + \sum_{k=1}^{\infty}\boldsymbol{E}_d^{(k)} \tag{82}$$

where

$$\begin{aligned} \boldsymbol{E}_d^{(k)}(\boldsymbol{r}) &= \int_V d^3\boldsymbol{r}G(\boldsymbol{r}-\boldsymbol{r}')U(\boldsymbol{r})\boldsymbol{E}_d^{(k-1)} = \\ &= \int_V d^3\boldsymbol{r}_1\ldots\int_V d^3\boldsymbol{r}_k G(\boldsymbol{r}-\boldsymbol{r}_1)U(\boldsymbol{r}_1)\ldots G(\boldsymbol{r}-\boldsymbol{r}_k)U(\boldsymbol{r}_k)\boldsymbol{E}_p(\boldsymbol{r}_k) \end{aligned} \tag{83}$$

The iteration is initialized by $\boldsymbol{E}_d^{(0)}(\boldsymbol{r}) = \boldsymbol{E}_p(\boldsymbol{r})$. It is evident that the *k*th order term in the solution is of the same order of magnitude as $\left(\tilde{\varepsilon}(\boldsymbol{r}')/\varepsilon_0\right)^k$. Therefore, consistently with the weak modulation assumption, only the first term is non-negligible. This assumption is called Born's approximation. The diffracted field is then expressed as

$$\boldsymbol{E}_d(\boldsymbol{r}) = \int_V d^3\boldsymbol{r}G(\boldsymbol{r}-\boldsymbol{r}')U(\boldsymbol{r})\boldsymbol{E}_p(\boldsymbol{r}) \tag{84}$$

6.2 Volume Diffraction of Scalar Fields

The actual computation of the diffracted field, as given by the diffraction integral (84), is not always straightforward. In this section we restrict the calculation to scalar fields and develop an approach based on 3D Fourier analysis, which simplifies many calculations and leads to the development of the k-sphere formulation. The key results of the present analysis are equation (92), which follows directly from (84) for scalar incident field, and (32), which is (92) rewritten in the Fourier domain.

Let us assume that the incident field is a plane wave linearly polarized parallel to an arbitrary direction $\hat{e}$, i.e.,

$$\boldsymbol{E}_p = \hat{e} e^{i\boldsymbol{k}_p \cdot \boldsymbol{r}} \qquad (\boldsymbol{k}_p \perp \hat{e}) \tag{85}$$

The diffracted field is then simply

$$\boldsymbol{E}_d(\boldsymbol{r}) = \int_V d^3\boldsymbol{r}' G(\boldsymbol{r}-\boldsymbol{r}') \tilde{\varepsilon}(\boldsymbol{r}) e^{i\boldsymbol{K}_g \cdot \boldsymbol{r}} \frac{(\boldsymbol{K}_g \cdot \hat{e})(-i\nabla + \boldsymbol{K}_g) + k^2}{\varepsilon_0} e^{i\boldsymbol{k}_p \cdot \boldsymbol{r}} \tag{86}$$

Green's dyadic for homogeneous space is

$$G(\boldsymbol{r}) = \frac{e^{ik_p r}}{4\pi r} I_3 \qquad \text{(outgoing waves only)} \tag{87}$$

where $k_p = 2\pi/\lambda = \left|\boldsymbol{k}_p\right|$ and I_3 is the 3x3 identity matrix. Substituting into () we obtain

$$\boldsymbol{E}_d(\boldsymbol{r}) = \boldsymbol{s}(\boldsymbol{k}_p) \int_V d^3\boldsymbol{r}' \frac{e^{ik_p|\boldsymbol{r}-\boldsymbol{r}'|}}{4\pi|\boldsymbol{r}-\boldsymbol{r}'|} \tilde{\varepsilon}(\boldsymbol{r}') e^{i(\boldsymbol{K}_g + \boldsymbol{k}_p)\boldsymbol{r}'} \tag{88}$$

where

$$\boldsymbol{s}(\boldsymbol{k}_p) = \frac{(\boldsymbol{K}_g \cdot \hat{e})(\boldsymbol{k}_p + \boldsymbol{K}_g) + k^2 \hat{e}}{\varepsilon_0} \tag{89}$$

Note that the diffracted field is also linearly polarized in the direction of $\hat{s}$. The angle α formed between $\hat{s}$ and the incident polarization $\hat{e}$ is given by

$$\cos\alpha = \hat{s}\cdot\hat{e} = \frac{\left(\boldsymbol{K}_g\cdot\hat{e}\right)^2 + k^2}{\sqrt{(\boldsymbol{K}_g\cdot\hat{e})^2\left(\left|\boldsymbol{K}_g\right|^2 + 2\boldsymbol{K}_g\cdot\boldsymbol{k}_p + k^2\right) + k^4}} \tag{90}$$

For a more general scalar incident field

$$\boldsymbol{E}_p(\boldsymbol{r}) = \hat{e}\tilde{E}_p(\boldsymbol{r})e^{i\boldsymbol{k}_p\cdot\boldsymbol{r}} \tag{91}$$

where $\tilde{E}_p(\boldsymbol{r})$ is the low bandwidth modulation, the diffracted field is

$$\boldsymbol{E}_d(\boldsymbol{r}) = \boldsymbol{s}(\boldsymbol{k}_p)\int_V d^3\boldsymbol{r}'\frac{e^{ik_p|\boldsymbol{r}-\boldsymbol{r}'|}}{4\pi|\boldsymbol{r}-\boldsymbol{r}'|}\tilde{\varepsilon}(\boldsymbol{r}')\tilde{E}_p(\boldsymbol{r}')e^{i\left(\boldsymbol{K}_g+\boldsymbol{k}_p\right)\boldsymbol{r}'} \tag{92}$$

This expression has a simple intuitive interpretation: each infinitesimal region inside the hologram acts as a point source with amplitude proportional to the local amplitude of the incident field and the local value of the refractive index modulation. The diffracted field is obtained as coherent superposition of the fields emitted by all these infinitesimal point sources comprising the volume hologram.

It will be useful in many subsequent calculations to have the Fourier-space equivalent of (92). For this purpose, we will now calculate the spatial spectrum of the diffracted field. To keep the notation simple, we adopt the convention that the optical axis is $\hat{\boldsymbol{z}}$, the transverse (to the optical axis) component of an arbitrary vector $\boldsymbol{v}$ is $v_\perp = \boldsymbol{v}\times\hat{\boldsymbol{z}}$, and the parallel component is $v_{||} = \boldsymbol{v}\cdot\hat{\boldsymbol{z}}$. We denote the Cartesian components of $\boldsymbol{v}$ as $v_{a|} = \boldsymbol{v}\cdot\hat{\boldsymbol{a}}$, where *a* is one of the *x*, *y*, or *z*, and $\hat{\boldsymbol{a}}$ is the corresponding unit vector $\hat{\boldsymbol{x}}$, $\hat{\boldsymbol{y}}$, or $\hat{\boldsymbol{z}}$ respectively. We define the diffracted spectrum as

$$\mathcal{E}_d(\boldsymbol{k}_d, z) = \int_{V_\perp} \boldsymbol{E}_d(\boldsymbol{r}) e^{-\boldsymbol{k}_d \cdot \boldsymbol{r}} d^2\boldsymbol{r}_\perp \tag{93}$$

and the inverse transform as

$$\boldsymbol{E}_d(\boldsymbol{r}) = \int \mathcal{E}_d(\boldsymbol{k}_d, z) e^{i\boldsymbol{k}_{d_\perp} \cdot \boldsymbol{r}} d\boldsymbol{k}_{d_\perp} \tag{94}$$

Here $V_\perp$ denotes the aperture of the hologram, and $\boldsymbol{k}_{d_\perp}$ refers to k_{dx} and k_{dy}. Substituting (88) into (94) and using the Fourier expansion of the Green's function,

$$\frac{e^{ik_p|\boldsymbol{r}-\boldsymbol{r}'|}}{4\pi|\boldsymbol{r}-\boldsymbol{r}'|} = \frac{i}{2}\int \frac{e^{i\boldsymbol{k}\cdot(\boldsymbol{r}-\boldsymbol{r}')}}{k_z} d^2\boldsymbol{k}_\perp \tag{95}$$

we obtain

$$\mathcal{E}_d(\boldsymbol{k}_d, z) = \frac{i\boldsymbol{s}(\boldsymbol{k}_p)}{2}\int\int_{V_\perp}\int_V d^3\boldsymbol{r}' d^2\boldsymbol{r}_\perp d^2\boldsymbol{k}_\perp \frac{e^{i(\boldsymbol{k}-\boldsymbol{k}_d)\cdot\boldsymbol{r}}}{k_{dz}} \tilde{\varepsilon}(\boldsymbol{r}') e^{i(\boldsymbol{K}_g+\boldsymbol{k}_p-\boldsymbol{k})\cdot\boldsymbol{r}'} \tag{96}$$

Performing the integration with respect to $\boldsymbol{r}_\perp$ yields $\delta(\boldsymbol{k}-\boldsymbol{k}_d)$; we then integrate with respect to $\boldsymbol{k}_\perp$ and obtain

$$\mathcal{E}_d(\boldsymbol{k}_d, z) = \frac{ie^{ik_{dz}z}}{2}\boldsymbol{A}(\boldsymbol{k}_p, \boldsymbol{k}_d) \tag{97}$$

$$\boldsymbol{A}(\boldsymbol{k}_p, \boldsymbol{k}_d) = \frac{\boldsymbol{s}(\boldsymbol{k}_p)}{k_{dz}}\int_V d^3\boldsymbol{r}' \tilde{\varepsilon}(\boldsymbol{r}') e^{i(\boldsymbol{K}_g+\boldsymbol{k}_p-\boldsymbol{k}_d)\cdot\boldsymbol{r}'} \tag{98}$$

The quantity $\boldsymbol{A}(\boldsymbol{k}_p, \boldsymbol{k}_d)$ is the three-dimensional Fourier transform of the index modulation $\tilde{\varepsilon}(\boldsymbol{r})e^{i\boldsymbol{K}_g\cdot\boldsymbol{r}}$, calculated at spatial frequency $\boldsymbol{k}_p - \boldsymbol{k}_d$. It represents the amplitude of the diffracted field propagating in the direction of $\hat{\boldsymbol{k}}_d$ when the hologram is illuminated by a plane wave incident at direction $\hat{\boldsymbol{k}}_p$. The diffracted electric field $\boldsymbol{E}_d$ can be calculated from $\boldsymbol{A}(\boldsymbol{k}_p, \boldsymbol{k}_d)$ as

$$\boldsymbol{E}_d(\boldsymbol{r}) = \frac{ie^{ikd_{dz}z}}{2k_{dz}} \iint \boldsymbol{A}(\boldsymbol{k}_p, \boldsymbol{k}_d) e^{ik_{dx}\cdot x} e^{ik_{dy}\cdot y} dk_x dk_y \tag{99}$$

We will use the formulation developed so far to calculate the field diffracted from a very simple volume hologram, recorded by the interference of two plane waves in a slab-like medium with thickness *L* in the $\hat{\boldsymbol{z}}$ direction. The general geometry is shown in Figure 8. In the notation of this chapter, $\boldsymbol{k}_f = \boldsymbol{k}_1$, $\boldsymbol{k}_s = \boldsymbol{k}_2$. During recording, the electric fields of the reference and signal beams are monochromatic plane waves

$$\boldsymbol{E}_f = \hat{\boldsymbol{y}} e^{ik(z\cos\theta_f - x\sin\theta_f)} \qquad \boldsymbol{E}_s = \hat{\boldsymbol{y}} e^{ik(z\cos\theta_s + x\sin\theta_s)} \tag{100}$$

The dielectric modulation is proportional to $\left|\boldsymbol{E}_f + \boldsymbol{E}_s\right|^2$. From the four interference terms, we need only maintain $\boldsymbol{E}_f^* \boldsymbol{E}_s$ (it can be shown that other terms do not contribute to diffraction here). Therefore

$$\tilde{\varepsilon}(\boldsymbol{r}) = \varepsilon_1 e^{i\boldsymbol{K}_g\cdot\boldsymbol{r}} rect\frac{z}{L} \tag{101}$$

where

$$\boldsymbol{K}_g = \boldsymbol{k}_s - \boldsymbol{k}_f = k(\sin\theta_s + \sin\theta_f)\hat{\boldsymbol{x}} + k(\cos\theta_s - \cos\theta_f)\hat{\boldsymbol{z}} \tag{102}$$

and ε_1 is a constant expressing the hologram strength ($\varepsilon_1 << \varepsilon_0$). The hologram is probed by a plane wave of the same wavelength

$$\boldsymbol{E}_p = \hat{\boldsymbol{y}} e^{ik(z\cos\theta_p - x\sin\theta_p)} \tag{103}$$

where $|\boldsymbol{k}_p| = k$, and θ_p is in general not equal to θ_f. That is we allow for Bragg-angle mismatched hologram readout. For later convenience, we define the "Bragg mismatch vector"

$$\delta\boldsymbol{k}_d = \boldsymbol{k}_p + \boldsymbol{K}_g - \boldsymbol{k}_d \tag{104}$$

in terms of the probe, grating and diffracted wave-vectors respectively. We now calculate

$$\boldsymbol{s}(\boldsymbol{k}_p) = \hat{\boldsymbol{y}}\frac{k^2}{\varepsilon_0} \tag{105}$$

and

$$\begin{aligned}\boldsymbol{A}(\boldsymbol{k}_p,\boldsymbol{k}_d) &= \hat{\boldsymbol{y}}\frac{k^2}{\varepsilon_0}\frac{\varepsilon_1}{k_{dz}}\int dx' e^{i(K_{gx}+k_{px}-k_{dx})x'}\int dy' e^{-ik_{dy}y'}\int dz' e^{i(K_{gz}+k_{pz}-k_{dz})z'} rect\frac{z'}{L} = \\ &= \hat{\boldsymbol{y}}\frac{k\varepsilon_1 L}{\varepsilon_0\cos\theta_d}\delta(K_{gx}+k_{px}-k_{dx})\delta(k_{dy})\mathrm{sinc}\left(\frac{L\hat{\boldsymbol{z}}\cdot\delta\boldsymbol{k}_d}{2\pi}\right)\end{aligned} \tag{106}$$

where $\mathrm{sinc}(u) \equiv \dfrac{\sin(\pi u)}{\pi u}$.

Using equation (99), we obtain the expression for the diffracted field, which is non-zero only if the transverse components of the diffracted wave-vector satisfy

$$k_{dx} = K_{gx} + k_{px} \qquad k_{dy} = 0 \tag{107}$$

We have also used the fact that $K_{gz} + k_{pz} - k_{dz} = (\boldsymbol{K}_g + \boldsymbol{k}_p - \boldsymbol{k}_d)\cdot\hat{\boldsymbol{z}} = \delta\boldsymbol{k}_d\cdot\hat{\boldsymbol{z}}$

The expression we obtain for the diffracted field is

$$\boldsymbol{E}_d(\boldsymbol{r}) = \hat{\boldsymbol{y}}\frac{ik\varepsilon_1 L}{2\varepsilon_0\cos\theta_d}\mathrm{sinc}\left(\frac{L\hat{\boldsymbol{z}}\cdot\delta\boldsymbol{k}_d}{2\pi}\right)e^{i\boldsymbol{k}_d\cdot\boldsymbol{r}} \tag{108}$$

Note that $\boldsymbol{k}_{d_\perp} = (k_{dx}, k_{dy}) = \boldsymbol{k}_d\times\hat{\boldsymbol{z}}$, so that we can write

$$\boldsymbol{k}_d\times\hat{\boldsymbol{z}} = (\boldsymbol{K}_g + \boldsymbol{k}_p)\times\hat{\boldsymbol{z}} \tag{109}$$

$$(\boldsymbol{K}_g + \boldsymbol{k}_p - \boldsymbol{k}_d)\times\hat{\boldsymbol{z}} = 0$$

$$\delta\boldsymbol{k}_d\times\hat{\boldsymbol{z}} = 0$$

We now present a geometrical construction, the k-sphere, which often

simplifies volume diffraction calculations. This construction, also known as the *Ewald* sphere, is familiar from crystallography and solid-state physics. The results that $\delta \boldsymbol{k}_d = |\delta \boldsymbol{k}_d| \hat{\boldsymbol{z}}$ and $|\boldsymbol{k}_d| = |\boldsymbol{k}_p| = k$ are interpreted as follows. The diffracted wave vector is constructed to have magnitude equal to that of the incident wave vector, and transverse component equal to the transverse component of the vectorial sum of the incident wave vector and the grating vector. In other words, the tip of the diffracted wave vector lies at the intersection of a sphere having radius equal to the magnitude of the incident wave vector with a line parallel to the z-axis passing also from the tip of the vectorial sum of the incident wave vector and the grating vector. For reference, Bragg-matched readout is shown in the diagram with dashed arrows.

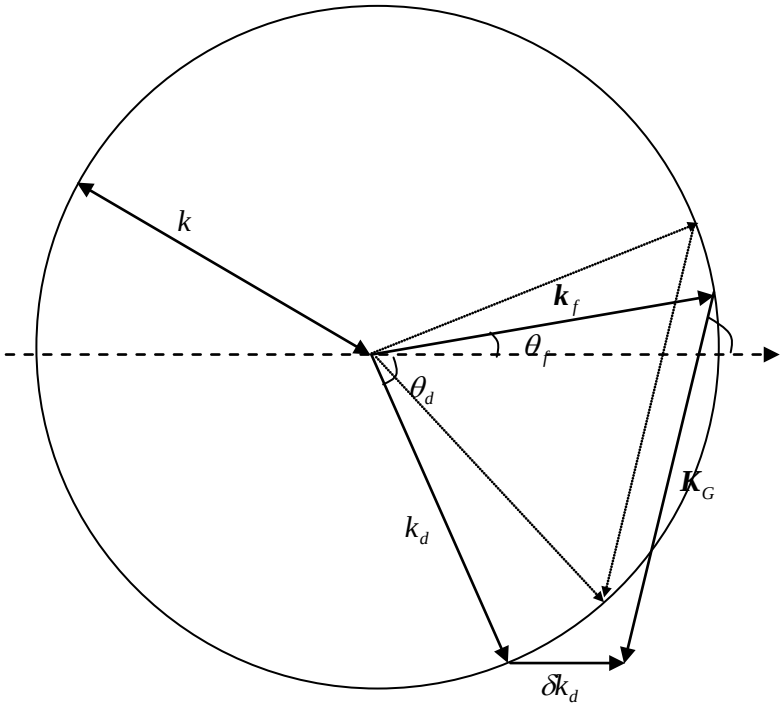

Figure 18. *Ewald* sphere for off-Bragg incidence

The diffraction efficiency, which expresses the proportion of incident intensity

diffracted by the hologram is

$$\eta = \frac{\left|\boldsymbol{E}_d\right|^2}{\left|\boldsymbol{E}_p\right|^2} = \left(\frac{\varepsilon_1 kL}{2\varepsilon_0 \cos\theta_d}\right)^2 \mathrm{sinc}^2\left(\frac{L\delta\boldsymbol{k}_d}{2\pi}\right) \tag{110}$$

That is, the diffraction efficiency is proportional to the sinc squared of the projection onto the z-axis of the vectorial sum of the incident wave vector and grating vector minus the diffracted wave vector, multiplied by the material thickness *L*. Thus the diffracted field is a plane wave propagating at an angle θ_d, and is attenuated by the Bragg mismatch factor given by the sinc function.

This result can also be arrived at from pure physical arguments. The diffracted beam is generated by the interaction of the electromagnetic field with the grating over a semi-infinite volume. The bandwidth-uncertainty product for the diffracted beam can be written as $\boldsymbol{\delta k}_d \cdot \Delta\boldsymbol{r} = 2\pi$, where $\boldsymbol{\delta k}_d$ represents the uncertainty in the diffracted beam wavevector k_d and $\Delta r = \Delta x\hat{x} + \Delta y\hat{y} + \Delta z\hat{z}$ represents the dimensions of the region of interaction. The grating is assumed to be infinite in the *x* and *y* directions, but has a finite thickness L in the *z*-direction ($\Delta x = \infty$, $\Delta y = \infty$, $\Delta z = L$). Therefore, the bandwidth uncertainty product implies that $\boldsymbol{\delta k}_{dx} = 0$, $\boldsymbol{\delta k}_{dy} = 0$, and $\boldsymbol{\delta k}_{dz} L = 2\pi$.

7 Coupled-Wave Theory for Thick Holographic Gratings

7.1 General Formulation

The coupled wave theory [9] assumes monochromatic light incident on the hologram grating at or near the Bragg angle and polarized perpendicular to the plane of incidence. Only two significant light waves are assumed to be present in the grating: the incoming “reference” wave R and the outgoing “signal” wave S. Only these two waves obey the Bragg condition at least approximately. The other diffraction orders violate the Bragg condition strongly and are neglected. They should be of little influence on the energy interchange between S and R.

Figure 8 shows the model of a hologram grating which is used for our analysis. The z-axis is chosen perpendicular to the surfaces of the medium, the x-axis is in the plane of incidence and parallel to the medium boundaries, and the y-axis is perpendicular to the paper. The fringe planes are oriented perpendicular to the plane of incidence and slanted with respect to the medium boundaries at an angle ϕ. The fringes are shown with dotted lines. The grating vector $\boldsymbol{K}$ is oriented perpendicular to the fringe planes and is of length $K = 2\pi/\Lambda$, where Λ is the period of the grating. The same average dielectric constant is assumed for the region inside and outside the grating boundaries. The angle of incidence measured in the medium is θ. We assume that the grating is immersed in a medium of the same average refractive index as that of the grating, so that there is no reflection and refraction at the boundaries.

7.1.1 Derivation of the Coupled Wave Equations

We restrict our attention to transmission lossless dielectric gratings, because gratings of this type are formed in the photorefractive poymer composites under study. Wave propagation in the grating is described by the scalar wave equation

$$\nabla^2 E + k^2 E = 0 \tag{111}$$

Where *E(x,z)* is the comlex amplitude of the *y*-component of the electric field, which is assumed to be independent of *y* and to oscillate with an angular frequency ω. The propagation constant *k(x,z)* is spatially modulated and related to the relative dielectric constant $\varepsilon(x,z)$ of the medium by

$$k^2 = \frac{\omega^2}{c^2}\varepsilon \tag{112}$$

where *c* is the light velocity in free space. In our model the constants of the medium are independent of *y*. The fringes of the hologram grating are represented by a spatial modulation of the dielectric constant

$$\varepsilon = \varepsilon_0 + \varepsilon_1 \cos(\boldsymbol{K}\cdot\boldsymbol{X}) \tag{113}$$

where ε_1 is the amplitude of the spatial modulation, ε_0 is the average dielectric constant. We have used the notation for the radius vector $\boldsymbol{X}$ and the grating vector $\boldsymbol{K}$

$$X = \begin{pmatrix} x \\ y \\ z \end{pmatrix}; \qquad \boldsymbol{K} = \begin{pmatrix} \sin\phi \\ 0 \\ \cos\phi \end{pmatrix}; \qquad K = 2\pi/\Lambda \tag{114}$$

Equations (112) and (113) can be combined in the form

$$k^2 = \beta^2 + 2\kappa\beta\left(e^{i\boldsymbol{K}\cdot\boldsymbol{X}} + e^{-i\boldsymbol{K}\cdot\boldsymbol{X}}\right) \tag{115}$$

where we have introduced the average propagation constant β

$$\beta = \frac{2\pi}{\lambda}\sqrt{\varepsilon_0} \tag{116}$$

and the coupling constant κ was defined as

$$\kappa = \frac{1}{4}\left(\frac{2\pi}{\lambda}\frac{\varepsilon_1}{\sqrt{\varepsilon_0}}\right) \tag{117}$$

This coupling constant describes the coupling between the reference wave *R* and the signal wave *S*. It is the central parameter in the coupled wave theory. For $\kappa = 0$ there is no coupling between *R* and *S* and, therefore, there is no diffraction. Since the average refractive index is $n_0 = \sqrt{\varepsilon_0}$, and the amplitude of the spatial modulation of the refractive index is $n_1 = \frac{\varepsilon_1}{2\sqrt{\varepsilon_0}}$, where $n_1 << n_0$, we can write with good accuracy

$$\beta = \frac{2\pi}{\lambda} n_0 \tag{118}$$

and

$$\kappa = \pi n_1 / \lambda \,, \tag{119}$$

where λ is the wavelength in free space.

The spatial modulation indicated by n_1 forms a grating, which couples the two waves *R* and *S* and leads to an exchange of energy between them. We describe these waves by complex amplitudes *R(z)* and *S(z)*, which vary along the z as a result of this energy interchange. The total electric field in the grating is the superposition of the two waves.

$$E = R(z)e^{-j\boldsymbol{\rho}\cdot\boldsymbol{X}} + S(z)e^{-j\boldsymbol{\sigma}\cdot\boldsymbol{X}} \tag{120}$$

The propagation vectors $\boldsymbol{\rho}$ and $\boldsymbol{\sigma}$ contain the information about the propagation constants and the directions of propagation of *R* and *S*. ρ is assumed to be equal to the propagation vector of the free reference wave in the absence of coupling. $\boldsymbol{\sigma}$ is forced by the grating and related to $\boldsymbol{\rho}$ and the grating vector by

$$\boldsymbol{\sigma} = \boldsymbol{\rho} - \boldsymbol{K} \tag{121}$$

which has the appearance of a conservation of momentum equation. $\boldsymbol{\rho}$ and $\boldsymbol{\sigma}$ have been chosen to confirm as closely as possible with our picture of the physical process of the diffraction in the grating. If the actual phase velocities differ somewhat from the assumed values, then these differences will appear in the complex amplitudes *R(z)* and *S(z)* as a result of the theory.

Figure 19(a) shows the vectors of interest and their orientation. The components of $\boldsymbol{\rho}$ are given as

$$\boldsymbol{\rho} = \begin{pmatrix} \rho_x \\ 0 \\ \rho_z \end{pmatrix} = \beta \begin{pmatrix} \sin\theta \\ 0 \\ \cos\theta \end{pmatrix} \tag{122}$$

From this and equation (121) follow the $\boldsymbol{\sigma}$ components

$$\boldsymbol{\sigma} = \begin{pmatrix} \sigma_x \\ 0 \\ \sigma_z \end{pmatrix} = \beta \begin{pmatrix} \sin\theta - \dfrac{K}{\beta}\sin\phi \\ 0 \\ \cos\theta - \dfrac{K}{\beta}\cos\phi \end{pmatrix} \tag{123}$$

The vector relation (121) is shown in Figure 19 together with Ewald sphere which is drawn on a plane as a circle of radius β. In principle, since there is no purely

monochromatic source in nature, the circle has a finite width. However, looking ahead, since our laser has a 5MHz linewidth, which for λ=532nm corresponds to $\Delta\beta = \Delta\lambda \frac{2\pi n}{\lambda^2} \approx 0.1m$, while $\beta \approx 10^7 m$. Therefore, the width of the β-circle can be safely neglected. The general case is shown in Figure 19(b), where the Bragg condition is not met and the length of $\boldsymbol{\sigma}$ differs from β. Bragg-matched diffraction is shown for reference with dotted arrows. From the triangle formed by the ρ, σ, and K vectors

$$\sigma^2 = \beta^2 + K^2 - 2\beta K \cos(\phi - \theta) \tag{124}$$

For Bragg-matched readout, the angle of incidence is θ_0. In this special case the lengths of both $\boldsymbol{\rho}$ and $\boldsymbol{\sigma}$ are equal to the free propagation constant β, and we have

$$\cos(\phi - \theta_0) = K/2\beta \tag{125}$$

For a fixed wavelength the Bragg condition is violated by angular deviation $\Delta\theta$ from the Bragg angle θ_0, and we write $\theta = \theta_0 + \Delta\theta$. In the case that we are interested in, $\Delta\theta$ is not much smaller than θ_0. For example, we will be considering a situation where $\Delta\theta$ is as high as 5^o and θ_0=35^o.

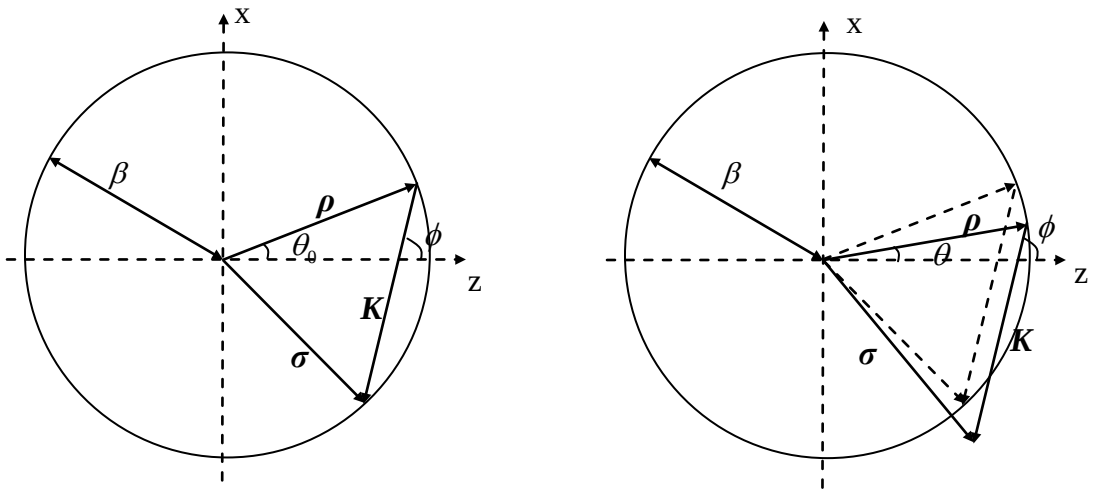

(a) (b)

Figure 19. (a) Bragg-matched readout and (b) Bragg-mismatched readout

We are now ready to derive the coupled wave equations. We combine (111) and (115) and insert expressions (120) and (121). The Laplacian of the E-field is

$$\nabla^2 E = (R'' - 2i\rho_z R' - \rho^2 R)e^{-i\boldsymbol{\rho}\cdot\boldsymbol{X}} + (S'' - 2i\sigma_z S' - \sigma^2 S)e^{-i\boldsymbol{\sigma}\cdot\boldsymbol{X}} \tag{126}$$

where the primes indicate differentiation with respect to *z*. Keeping in mind that $\rho^2 = \beta^2$, the Helmholtz equation becomes

$$\begin{aligned}(R'' - 2i\rho_z R')e^{-i\boldsymbol{\rho}\cdot\boldsymbol{X}} + [S'' - 2i\sigma_z S' + (\beta^2 - \sigma^2)S]e^{-i\boldsymbol{\sigma}\cdot\boldsymbol{X}} + \\ + 2\kappa\beta[R(e^{-i(\boldsymbol{\rho}-\boldsymbol{K})\cdot\boldsymbol{X}} + e^{-i(\boldsymbol{\rho}+\boldsymbol{K})\cdot\boldsymbol{X}}) + S(e^{-i(\boldsymbol{\sigma}-\boldsymbol{K})\cdot\boldsymbol{X}} + e^{-i(\boldsymbol{\sigma}+\boldsymbol{K})\cdot\boldsymbol{X}})] = 0\end{aligned} \tag{127}$$

The waves generated in the directions of $\boldsymbol{\rho}+\boldsymbol{K}$ and $\boldsymbol{\sigma}-\boldsymbol{K}$ are neglected together with all higher diffraction orders. Then we compare the terms with equal exponentials ($e^{-i\boldsymbol{\rho}\cdot\boldsymbol{X}}$ and $e^{-i\boldsymbol{\sigma}\cdot\boldsymbol{X}}$) and arrive at

$$R'' - 2jR'\rho_z + 2\kappa\beta S = 0 \tag{128}$$

$$S'' - 2jS'\sigma_z + (\beta^2 - \sigma^2)S + 2\kappa\beta R = 0$$

In addition, we assume that the energy interchange between *S* and *R* is slow. This allows us to neglect R'' and S'' (slowly varying envelope approximation). We will check the results of the theory later for a more detailed justification of this last step. We can now write the above equations in the form

$$\frac{\rho_z}{\beta} R' = -i\kappa S \tag{129}$$

$$\frac{\sigma_z}{\beta} S' + i\frac{\beta^2 - \sigma^2}{2\beta} S = -i\kappa R$$

Next we introduce the obliquity parameters c_R and c_S

$$c_R = \rho_z / \beta = \cos\theta \tag{130}$$

$$c_S = \sigma_z / \beta = \cos\theta - \frac{K}{\beta}\cos\phi \tag{131}$$

and the dephasing measure ϑ defined by

$$\vartheta \equiv \left(\beta^2 - \sigma^2\right)/2\beta \tag{132}$$

The $\theta - \lambda$ connection shows up in the dephasing measure ϑ, which can also be expressed as

$$\vartheta \equiv K\cos(\phi - \theta) - \frac{K^2}{4\pi n}\lambda \tag{133}$$

We can now write the coupled-wave equations, which are the basis of our analysis

$$c_R R' = -j\kappa S \tag{134}$$

$$c_S S' + j\vartheta S = -j\kappa R$$

Our physical picture of diffraction process is reflected in the coupled wave equations. A wave changes in amplitude along z because of coupling to the other wave (κR or κS). For deviations from the Bragg condition S is forced out of synchronism with R and the interaction decreases (ϑS).

Multiplying the first equation in (133) by R^* and the second by S^*, and adding the results together with their complex conjugates, we obtain the energy balance of the coupled-wave model

$$\frac{d}{dz}(c_R RR^* + c_S SS^*) = 0 \tag{135}$$

The reference wave R is assumed to start with unit amplitude at $z=0$. It decays as it propagates to the right and coupled energy into S. In transmission holograms the signal S starts out with zero amplitude at z=0 and propagates to the right ($c_S > 0$). Therefore, the boundary conditions are

$$R(0) = 1, \quad S(0) = 0 \tag{136}$$

so that the energy balance equation can be written as

$$|R(z)|^2 + \frac{c_S}{c_R}|S(z)|^2 = 1 \tag{137}$$

The presence of the obliquity factors c_R and c_S indicates that it is the power flow of the two waves in the z direction that enters the energy balance. In the absence of loss, this power is conserved.

7.1.2 Solution of the Coupled Wave Equations

It is straightforward to obtain the general solution of the coupled wave equations. We take an ansatz solution of the form

$$R(z) = r_1 e^{\gamma_1 z} + r_2 e^{\gamma_2 z} \tag{138}$$

$$S(z) = s_1 e^{\gamma_1 z} + s_2 e^{\gamma_2 z} \tag{139}$$

Where r_i and s_i are constants which depend on the boundary conditions. To determine the constants γ_i we insert equations (137) and (138) into the coupled wave equations and obtain

$$c_R \gamma_i r_i = -j\kappa s_i \tag{140}$$

$$(c_S \gamma_i + j\vartheta) s_i = -j\kappa r_i \tag{141}$$

where i=1,2. After multiplying the equations with each other we get a quadratic equation for γ_i

$$c_R \gamma_i (c_S \gamma_i + j\vartheta) = -\kappa^2 \tag{142}$$

with the solution

$$\gamma_{1,2} = -j\frac{\vartheta}{2c_S} \pm j\sqrt{\frac{\vartheta^2}{4c_S^2} + \frac{\kappa^2}{c_R c_S}} \tag{143}$$

At this point we divert briefly from the main derivation, because now we have the means to check the validity of neglecting R'' and S'' in the coupled wave equations. This step is justified if the conditions $R'' << \rho_z R'$ and $S'' << \sigma_z S'$ are obeyed. We have

$$R' = \sum \gamma_i r_i e^{\gamma_i z}, \qquad S' = \sum \gamma_i s_i e^{\gamma_i z} \tag{143}$$

$$R'' = \sum \gamma_i^2 r_i e^{\gamma_i z}, \qquad S'' = \sum \gamma_i^2 s_i e^{\gamma_i z}$$

so that the second-order derivatives can be neglected if $\gamma_i << \beta$. If $\Delta\theta << 1$, then $\vartheta << 1$

and $\gamma_i \approx \frac{\kappa}{\sqrt{c_R c_S}} = \frac{\pi n_1}{\lambda}\frac{1}{\sqrt{c_R c_S}} = \frac{n_1}{n_0}\frac{2\pi n_0}{\lambda}\frac{1}{\sqrt{c_R c_S}} = \frac{n_1}{n_0}\frac{\beta}{\sqrt{c_R c_S}} << \beta$ because $n_1 << n_0$.

However, if $\Delta\theta$ is not very small, the case is not so clear. Looking ahead, using our experimental data, we calculate γ for the case of a grating written by laser beams at $\lambda = 532nm$ incident at 35^o and 20^o from the same side of the z-axis, and we measured $n_1 = 3\times10^{-4}$. The read angle is 35^o, and we consider the case of largest deviation of $\Delta\theta = 5^o$ from the Bragg angle. We obtain the ratio $\frac{\gamma}{\beta} \approx 10^{-2}$, which says that the second order derivatives can still be neglected. However, it should be pointed out that there may exist circumstances when one has to keep the higher order derivatives, so that the coupled wave equations are

$$\frac{j}{2\beta}R'' + c_R R' = -j\kappa S \tag{144}$$

$$\frac{j}{2\beta}S'' + c_S S' + j\vartheta S = -j\kappa R$$

Continuing the coupled wave analysis, if we insert the boundary conditions into equations (140) and (141), it follows immediately that

$$r_1 + r_2 = 1 \tag{145}$$

$$s_1 + s_2 = 0$$

Combining these relations with equation (140) we obtain

$$s_1 = -s_2 = -j\frac{\kappa}{c_S(\gamma_1 - \gamma_2)} \tag{146}$$

Introducing these constants in equation (139) we arrive at an expression for the amplitude of the signal wave at the output of the grating ($z=L$)

$$S(L) = j\frac{\kappa}{c_S(\gamma_1 - \gamma_2)}(e^{\gamma_2 L} - e^{\gamma_1 L}) \tag{147}$$

For simplicity of notation, let us introduce the following:

$$\gamma_i = -j\xi \pm j\sqrt{\xi^2 + \nu^2} \tag{148}$$

where

$$\nu = \frac{\kappa}{\sqrt{c_R c_S}} = \frac{\pi n_1}{\lambda\sqrt{c_R c_S}} \tag{149}$$

and

$$\xi = \frac{\vartheta}{2c_S} \tag{150}$$

The final expression for the diffracted signal wave at $z=L$ is

$$S(L) = -j\sqrt{\frac{c_R}{c_S}}e^{-j\xi d}\frac{\sin\left(\sqrt{\xi^2 + \nu^2}L\right)}{\sqrt{1+\xi^2/\nu^2}} \tag{151}$$

To derive the expression for the reference wave at $z=L$, recall that

$$\begin{aligned} c_R\gamma_1 r_1 &= -j\kappa s_1 \qquad & r_1 + r_2 &= 1 \\ c_R\gamma_1 r_1 &= -j\kappa s_1 \qquad & s_1 + s_2 &= 0 \end{aligned} \tag{152}$$

From these we obtain

$$r_1 = \frac{\gamma_2}{\gamma_2 - \gamma_1}\ , \qquad r_2 = \frac{\gamma_1}{\gamma_1 - \gamma_2} \tag{153}$$

Therefore, we have

$$R(z) = \frac{1}{\gamma_1 - \gamma_2}\left(\gamma_1 e^{\gamma_2 z} - \gamma_2 e^{\gamma_1 z}\right) \tag{154}$$

which can be written in the final form as

$$R(L) = e^{-j\xi d}\left(j\frac{\xi}{\sqrt{\xi^2+\nu^2}}\sin\left(\sqrt{\xi^2+\nu^2}L\right) + \cos\left(\sqrt{\xi^2+\nu^2}L\right)\right) \tag{155}$$

We can now verify the conservation of energy

$$|R(L)|^2 = \frac{\xi^2}{\xi^2+\nu^2}\sin^2\left(\sqrt{\xi^2+\nu^2}L\right) + \cos^2\left(\sqrt{\xi^2+\nu^2}L\right) \tag{156}$$

and

$$|S(L)|^2 = \frac{c_S}{c_R}\frac{\sin^2\left(\sqrt{\xi^2+\nu^2}L\right)}{1+\xi^2/\nu^2} \tag{157}$$

so that

$$|R(L)|^2 + \frac{c_R}{c_S}|S(L)|^2 = 1 \tag{158}$$

In our discussion, the parameter of prime interest is the diffraction efficiency η, which is defined as

$$\eta = \frac{c_S}{c_R}|S(L)|^2 \tag{159}$$

where *S* is the (complex) amplitude of the output signal for a reference wave *R* incident with unit amplitude. η is the fraction of the incident light power which is diffracted into the signal wave. The obliquity factors c_R and c_S appear in the above definition for the same reason they have appeared in the energy balance of equation (137): in the absence of loss it is the power flow in the z-direction which is conserved. The diffraction

efficiency formula now is

$$\eta = \frac{\sin^2\left(\sqrt{\xi^2 + \nu^2}L\right)}{1 + \xi^2/\nu^2} \tag{160}$$

It is not straightforward to prove algebraically that the diffraction efficiency formula derived from the Born approximation and coupled-wave theories are equivalent. However, numerical evaluations for four materials of different thickness, in each case have produced almost identical results for the of diffraction efficiency dependence on angular deviation from the Bragg angle.

Note that the coupled wave theory predicts that inside the gratings there is a continuous flow of energy between *R* and *S*, which is equivalent to the behavior of two coupled oscillators. This effect is not predicted by the diffraction in the Born approximation theory. For Bragg-matched incidence $\xi = 0$, so that for $0 \le z \le L$

$$|R(z)|^2 = \cos^2(\nu z) \tag{161}$$

$$\frac{c_s}{c_R}|S(z)|^2 = \sin^2(\nu z)$$

Figure 20 shows the beam powers $|R(z)|^2$ and $(c_S/c_R)|S(z)|^2$ versus *z* for a holographic material of length L =2.5mm, n_0=1.6, $n_1 = 3\times10^4$, $\lambda = 532$ nm, $\theta_0 = 35^o$, and a grating with $\Lambda = 1.3\,\mu$m and $\phi = 65^o$

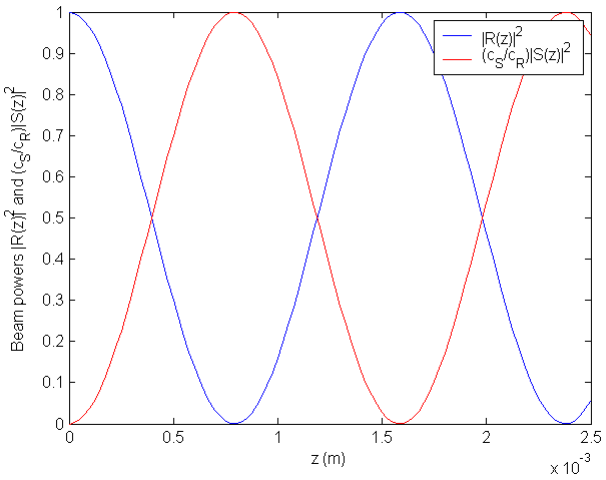

Figure20. Beam powers $|R(z)|^2$ and $(c_S/c_R)|S(z)|^2$ versus z in phase-matched Bragg diffraction

Figure 21 shows beam powers for off-Bragg incidence with $\Delta\theta = 10\,\text{mrad}$, where the beam powers are calculated using the following equations

$$|R(z)|^2 = \frac{\xi^2}{\xi^2+\nu^2}\sin^2\left(\sqrt{\xi^2+\nu^2}\,z\right) + \cos^2\left(\sqrt{\xi^2+\nu^2}\,z\right) \tag{162}$$

$$\frac{c_S}{c_R}|S(z)|^2 = \frac{\sin^2\left(\sqrt{\xi^2+\nu^2}\,z\right)}{1+\xi^2/\nu^2}$$

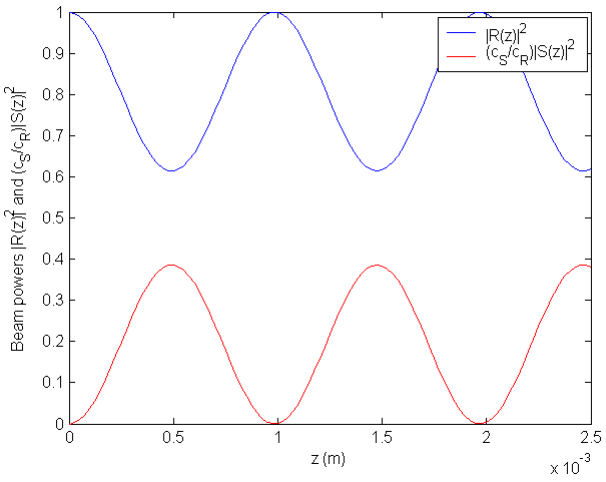

Figure 21. Beam powers $|R(z)|^2$ and $(c_S/c_R)|S(z)|^2$ versus z in Bragg-mismatched diffraction with $\Delta\theta = 10$ mrad

Inspection of Figure 21 reveals that power transfer is not complete. The Bragg-mismatched readout corresponds to the system of two coupled oscillators with off-resonant excitation.

7.1.3 Consistency with Conservation of Energy and Momentum

We now shift our attention to the question of the direction of the diffracted beam S for off-Bragg incidence [48]. Recall that the total scalar electric field was defined as

$$E = R(z)e^{-j\boldsymbol{\rho}\cdot\boldsymbol{X}} + S(z)e^{-j\boldsymbol{\sigma}\cdot\boldsymbol{X}} \tag{120}$$

We defined the diffracted wave vector by

$$\boldsymbol{\sigma} = \boldsymbol{\rho} - \boldsymbol{K} \tag{121}$$

with the provision that additional corrective factors to the wavevector may appear in the final expressions for the complex amplitudes $R(z)$ and $S(z)$ as a result of the

theory. Indeed, both *R(z)* and *S(z)* contain a phase factor $e^{-j\xi z}$. This phase factor identifies the vector $\boldsymbol{\xi}$

$$\boldsymbol{\xi} = \frac{\vartheta}{2c_S} = \frac{\beta^2 - \sigma^2}{4\sigma_z}\hat{\boldsymbol{z}} \tag{163}$$

to be a correction to the initial guess of the $\boldsymbol{\sigma}$ vector, so that the actual wavevector of the diffracted beam as predicted by the coupled-wave theory is

$$\boldsymbol{\sigma}' = \boldsymbol{\rho} - \boldsymbol{K} + \boldsymbol{\xi} \tag{164}$$

Just as the $\delta\boldsymbol{k}_d$ mismatch vector in the Born approximation theory (Chapter 6.2), $\boldsymbol{\xi}$ points in the *z*-direction, which is also consistent with the bandwidth-uncertainty product requirement as a consequence of the finite thickness of the grating in the z-direction. One can see from Figure 22 that in the Bragg-mismatched case, $\sigma \neq \beta$, which is a violation of the conservation of energy. Note that if $\sigma > \beta$, then $\boldsymbol{\xi}$ is pointing in the $-\hat{\boldsymbol{z}}$ direction, and if $\sigma < \beta$ then $\boldsymbol{\xi}$ is pointing in the $+\hat{\boldsymbol{z}}$. That is, $\boldsymbol{\xi}$ is acting to bring the tip of the $\boldsymbol{\sigma}$-vector back to the β-circle. Let us compare the magnitude of the $\boldsymbol{\xi}$ vector with the magnitude of the $\delta\boldsymbol{k}_d$ vector from the Born approximation theory. Considering the case of off-Bragg incidence shown in Figure 22. From the triangle formed by vectors $\boldsymbol{k}_d$, $\delta\boldsymbol{k}_d$ and $\boldsymbol{\sigma}$, where $|\boldsymbol{k}_d| = \beta$ and $|\delta\boldsymbol{k}_d| = \Delta\sigma$, the law of cosines gives

$$\beta^2 = \sigma^2 + (\Delta\sigma)^2 - 2\sigma(\Delta\sigma)\cos(\varphi) \tag{165}$$

but

$$\cos\varphi = \sigma_z / \sigma \tag{166}$$

therefore, we obtain a quadratic equation

$$(\Delta\sigma)^2 - 2(\Delta\sigma)\sigma_z + (\sigma^2 - \beta^2) = 0 \tag{167}$$

with the solution

$$\Delta\sigma_{1,2} = \sigma_z \pm \sqrt{\sigma_z^2 - (\sigma^2 - \beta^2)} \tag{168}$$

The solution with the + sign can be dropped because it corresponds to the distance to the opposite side of the circle. Writing the solution in the form

$$\Delta\sigma = \sigma_z - \sigma_z\sqrt{1 - \frac{\sigma^2 - \beta^2}{\sigma_z^2}} \tag{169}$$

we note that $\frac{\sigma^2 - \beta^2}{\sigma_z^2} << 1$. For example, for the 16μm photorefractive polymer sample at the largest deviation of $\Delta\theta = 5^o$, we have $\frac{\sigma^2 - \beta^2}{\sigma_z^2} \approx 0.05$. Therefore, we have

$$\Delta\sigma \approx \frac{\sigma^2 - \beta^2}{2\sigma_z} \tag{170}$$

so that

$$\xi \approx \frac{\Delta\sigma}{2} \tag{171}$$

Hence the tip of the vector $\boldsymbol{\sigma}'$ is not on the β-circle. Note that since the expression for *R(z)* also contains the phase factor $e^{-j\xi z}$, the coupled wave theory predicts that the propagation vectors of the reference wave after the gratings is

$$\boldsymbol{\rho}' = \boldsymbol{\rho} + \boldsymbol{\xi} \tag{172}$$

That is $|\boldsymbol{\sigma}'| \neq \beta$ and $|\boldsymbol{\rho}'| \neq \beta$, which is inconsistent with our understanding of the physical process.

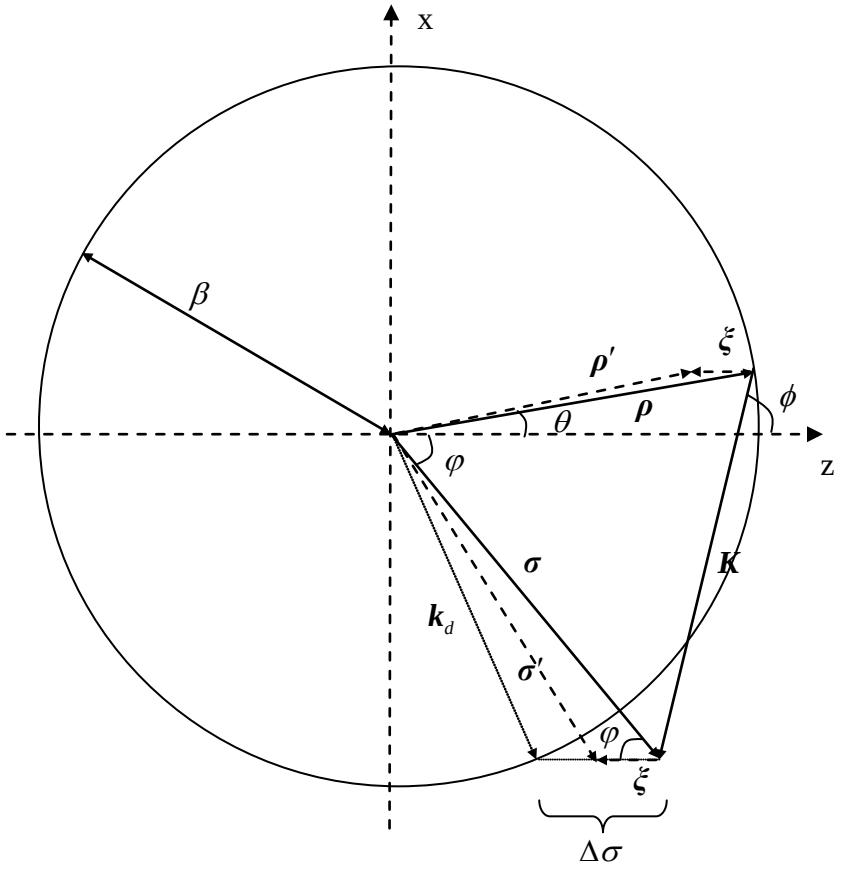

Figure 22. Corrected wavevectors of the incident and diffracted beams

7.2 Coupled-Wave Theory with Forced Mismatch Vector

There exists an approach to coupled-wave theory that attempts to resolve the controversy with the mismatch of the diffracted wavevector for off-Bragg incidence by explicitly assuming that [35]

$$|\boldsymbol{\sigma}| = \beta \tag{173}$$

and

$$\boldsymbol{\sigma} = \boldsymbol{\rho} - \boldsymbol{K} + \Delta\boldsymbol{\sigma} \tag{174}$$

Here $\Delta\boldsymbol{\sigma}$ is assumed to be pointing in the *z*-direction. Comparing with the Born approximation theory, $\boldsymbol{\sigma} = \boldsymbol{k}_d$ and $\Delta\boldsymbol{\sigma} = \delta\boldsymbol{k}_d$. However, we will show that the solution of the coupled-wave equations will produce additional phase corrections to $\boldsymbol{\sigma}$ and $\boldsymbol{\rho}$, resulting in violation of conservation of energy. To proceed with the coupled wave analysis using the new assumptions about the wavevectors, recall equation (127) that now has the form

$$\begin{aligned}(R'' - 2i\rho_z R')e^{-i\boldsymbol{\rho}\cdot\boldsymbol{X}} + (S'' - 2i\sigma_z S')e^{-i\boldsymbol{\sigma}\cdot\boldsymbol{X}} + \\ + 2\kappa\beta[R(e^{-i(\boldsymbol{\rho}-\boldsymbol{K})\cdot\boldsymbol{X}} + e^{-i(\boldsymbol{\rho}+\boldsymbol{K})\cdot\boldsymbol{X}}) + S(e^{-i(\boldsymbol{\sigma}-\boldsymbol{K})\cdot\boldsymbol{X}} + e^{-i(\boldsymbol{\sigma}+\boldsymbol{K})\cdot\boldsymbol{X}})] = 0\end{aligned} \tag{175}$$

As before, the waves generated in the directions of $\boldsymbol{\rho} + \boldsymbol{K}$ and $\boldsymbol{\sigma} - \boldsymbol{K}$ are neglected together with all higher diffraction orders. However, now $\boldsymbol{\rho} - \boldsymbol{K} = \boldsymbol{\sigma} - \Delta\boldsymbol{\sigma}$ and $\boldsymbol{\sigma} + \boldsymbol{K} = \boldsymbol{\rho} + \Delta\boldsymbol{\sigma}$. Therefore, when we group the terms with equal exponentials ($e^{-i\boldsymbol{\rho}\cdot\boldsymbol{X}}$ and $e^{-i\boldsymbol{\sigma}\cdot\boldsymbol{X}}$), we arrive at

$$\begin{aligned}R'' - 2jR'\rho_z + 2\kappa\beta S e^{-j\Delta\sigma z} = 0 \\ S'' - 2jS'\sigma_z + 2\kappa\beta R e^{j\Delta\sigma z} = 0\end{aligned} \tag{176}$$

Using the same reasons as before, we drop the second order derivatives, so that the coupled-wave equations are

$$\begin{aligned}c_R R' = -j\kappa S e^{-j\Delta\sigma z} \\ c_S S' = -j\kappa R e^{j\Delta\sigma z}\end{aligned} \tag{177}$$

where $c_R = \rho_z/\beta$ and $c_S = \sigma_z/\beta$ as defined before. Carrying out a differentiation with respect to *z* on both sides of the first equation

$$c_R R'' = -j\kappa(S' - j\Delta\sigma S)e^{-j\Delta\sigma z} \tag{178}$$

but

$$S = j\frac{c_R}{\kappa}R'e^{j\Delta\sigma z} \tag{179}$$

and using the second equation

$$S' = -j\frac{\kappa}{c_S}Re^{j\Delta\sigma z} \tag{180}$$

we arrive at the following differential equation

$$R'' + j\Delta\sigma R' + \nu^2 R = 0 \tag{181}$$

where $\nu = \kappa/\sqrt{c_R c_S}$ as defined previously. Taking an ansatz solution in the form $e^{\gamma z}$, we obtain a quadratic equation in γ with a solution

$$\gamma_{1,2} = -j\frac{\Delta\sigma}{2} \pm \sqrt{\left(\frac{\Delta\sigma}{2}\right)^2 + \nu^2} \tag{182}$$

Recall from the previous section that we had a parameter ξ defined as $\xi \equiv \frac{\vartheta}{2c_S}$, and that $\xi \approx \frac{\Delta\sigma}{2}$, so that

$$\gamma_{1,2} \approx -j\xi \pm \sqrt{\xi^2 + \nu^2} \tag{183}$$

as in the previous section.

Continuing with our analysis, for simplicity of notation, let us introduce a new parameter

$$\chi = \sqrt{(\Delta\sigma/2)^2 + \nu^2}\,. \tag{184}$$

A general solution to the equation (181) is given by

$$R(z) = e^{-j\frac{\Delta\sigma}{2}z}[C_1 \sin(\chi z) + C_2 \cos(\chi z)] \tag{185}$$

where C_1 and C_2 are constants. Solution for $S(z)$ is obtained using equations () and () and is given by

$$S(z) = e^{j\frac{\Delta\sigma}{2}z}\left[\left(\frac{\Delta\sigma}{2}\frac{c_R}{\kappa}C_1 - j\frac{c_R}{\kappa}\tau C_2\right)\sin(\chi z) + \left(j\frac{c_R}{\kappa}\tau C_1 + \frac{\Delta\sigma}{2}\frac{c_R}{\kappa}C_2\right)\cos(\chi z)\right] \tag{186}$$

The constants C_1 and C_2 are determined by the initial conditions $R(0)=1$ and $S(0)=0$. The constants are

$$C_1 = j\frac{\Delta\sigma}{2\tau} \tag{187}$$

$$C_2 = 1 \tag{188}$$

Substitution of these constants into equations (185) and (186), after some algebraic manipulations leads to

$$R(z) = e^{-j\frac{\Delta\sigma}{2}z}\left[j\frac{\Delta\sigma}{2\sqrt{(\Delta\sigma/2)^2+\nu^2}}\sin\left(\sqrt{(\Delta\sigma/2)^2+\nu^2}\,z\right) + \cos\left(\sqrt{(\Delta\sigma/2)^2+\nu^2}\,z\right)\right] \tag{189}$$

$$S(z) = e^{j\frac{\Delta\sigma}{2}z}\left[-j\sqrt{\frac{c_R}{c_S}}\frac{\nu}{\sqrt{(\Delta\sigma/2)^2+\nu^2}}\sin\left(\sqrt{(\Delta\sigma/2)^2+\nu^2}\,z\right)\right]$$

Using the condition $\xi \approx \frac{\Delta\sigma}{2}$ leads to the familiar expressions

$$R(z) \approx e^{-j\xi z}\left[j\frac{\xi}{\sqrt{\xi^2+\nu^2}}\sin\left(\sqrt{\xi^2+\nu^2}\,z\right) + \cos\left(\sqrt{\xi^2+\nu^2}\,z\right)\right] \tag{190}$$

$$S(z) \approx -je^{j\xi z}\sqrt{\frac{c_R}{c_S}}\frac{1}{\sqrt{\xi^2+\nu^2}}\sin\left(\sqrt{\xi^2+\nu^2}\,z\right)$$

with the only difference that unlike in the previous section, the phases of *R(z)* and *S(z)* are of the opposite sign. All previously derived relations for the diffraction efficiency and conservation of power flow in the z-direction therefore apply here as well. However, just as before, the phases of *S(z)* and *R(z)* introduce corrections to the initially defined wavevectors. The corrected wavevectors are

$$\boldsymbol{\rho}' = \boldsymbol{\rho} + \frac{\Delta\boldsymbol{\sigma}}{2} \tag{191}$$

$$\boldsymbol{\sigma}' = \boldsymbol{\rho} - \boldsymbol{K} + \Delta\boldsymbol{\sigma} - \frac{\Delta\boldsymbol{\sigma}}{2} = \boldsymbol{\rho} - \boldsymbol{K} + \frac{\Delta\boldsymbol{\sigma}}{2} \tag{192}$$

For the case sketched in Figure 22 $\Delta\boldsymbol{\sigma}$ points in the $-z$ direction, so that just as before, the tips of neither $\boldsymbol{\rho}'$ nor $\boldsymbol{\sigma}'$ vectors are on the β-circle. The wavevectors obtained from the coupled-wave theory in Chapter 7.1 and corrected coupled-wave theory in Chapter 7.2 are identical.

8 Holographic Image Recognition System

8.1 Spatio-Angular Multiplexed Holographic Memory

In many military as well as civilian applications, rapid target identification is essential. Targets are identified by comparing an incoming image with a database of target images, i.e., by correlating the images. Current image correlation techniques rely upon digital signal processing (DSP) elements that are often too slow for target intercept applications because the data is compared serially**.** Optical image correlation techniques possess a tremendous potential advantage in speed because of inherent parallelism in optics. In principle, a huge database of images, accounting for shift, scale and rotation variance of every image, is needed for reliable identification of the target. Shift-invariant correlation can be implemented in the Fourier plane, owing to the shift-invariant property of the Fourier Transform. The optical spatial Fourier Transform is produced trivially by a thin lens at its back focal plane. Utilizing certain algorithms, such as the rotationally invariant Fourier-Mellin transform, may further reduce the size of the required database [49]. However, unlike the Fourier Transform case, implementation of such algorithms requires electronic pre-processing, which slows down the correlation process. We propose to accomplish fast rotation and scale-invariant correlation by performing a very time-efficient optical exhaustive search of a large holographic image database. Massive holographic memory can be realized by multiplexing techniques, aimed at achieving dense holographic storage. Spatio-angular multiplexing (SAM) is the most straightforward and effective technique, and several approaches [50-52], including one

from our group [53-55], have been presented for constructing SAM holographic memory.

The basic idea of our spatio-angular multiplexed architecture that we called a super-parallel holographic memory is illustrated in Figure 23. Briefly, the holographic memory unit (HMU) is recorded with the database of interest, using multiple spatial locations, each of which contains a set of images that are angularly multiplexing in two dimensions. When operating the memory system, the user enters as coordinates the spatial position and the angle of storage of the image of interest. The position coordinate is used to open the corresponding element of a shutter array. The number of elements in the shutter array is the same as the number of spatial locations in the HMU, and the locations are matched. Shutter arrays of this type are available commercially, with individually addressable ferroelectric liquid crystals, for example, with a very fast switching time and high extinction ratio. MEMS based microdeflectors can also be used for this shutter array, which will have a virtually perfect extinction. (Alternatively, the shutter array can be eliminated from this architecture if one uses a two-photon memory, where only the location of interest is illuminated by the activation laser frequency.)

The angular coordinate for the image is sent to a beam deflector (e.g., using a pair of acousto-optic or electro-optic deflectors), which orients the read beam at the desired angle, which in turn is translated to a specific position by the redirector. A combination of the reducing telescope, the multiplexer, the redirector, and the lenslet array produces a copy of the read beam simultaneously at each of the locations. As such, the image stored at this angle will be recalled from each location. The shutter array will block all but one of these images, and the redirector and the demultiplexer will send the wanted image to

the CCD camera.

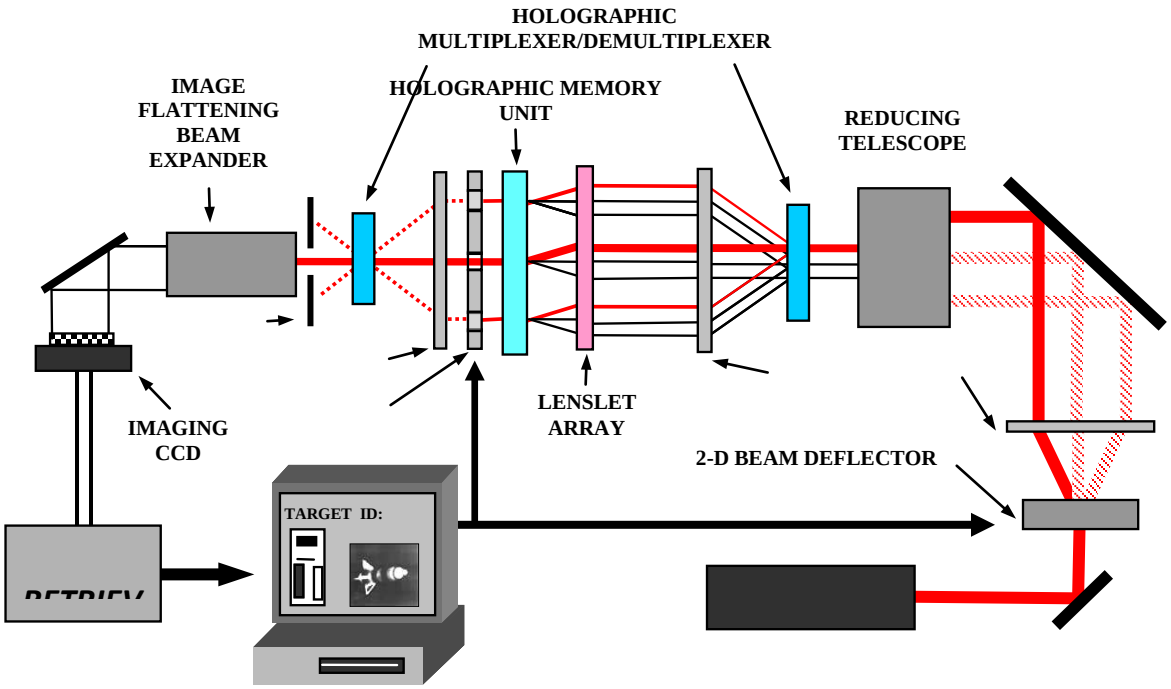

Figure 23**.** Schematic illustration of the Super-Parallel Holographic Memory (SPHM) architecture.

We have recently demonstrated the feasibility of one part of this concept here, by using a pair of galvo-mounted mirrors for deflections [54]. The geometry used by us for the demonstration is shown in Figure 24. For the database, we used an HMU that has 9 locations, in a 3X3 arrangement, each location containing 8 images multiplexed angularly. The bottom of the figure shows a typical set of data retrieved using this setup. Similar data were also retrieved from the other locations (not shown).

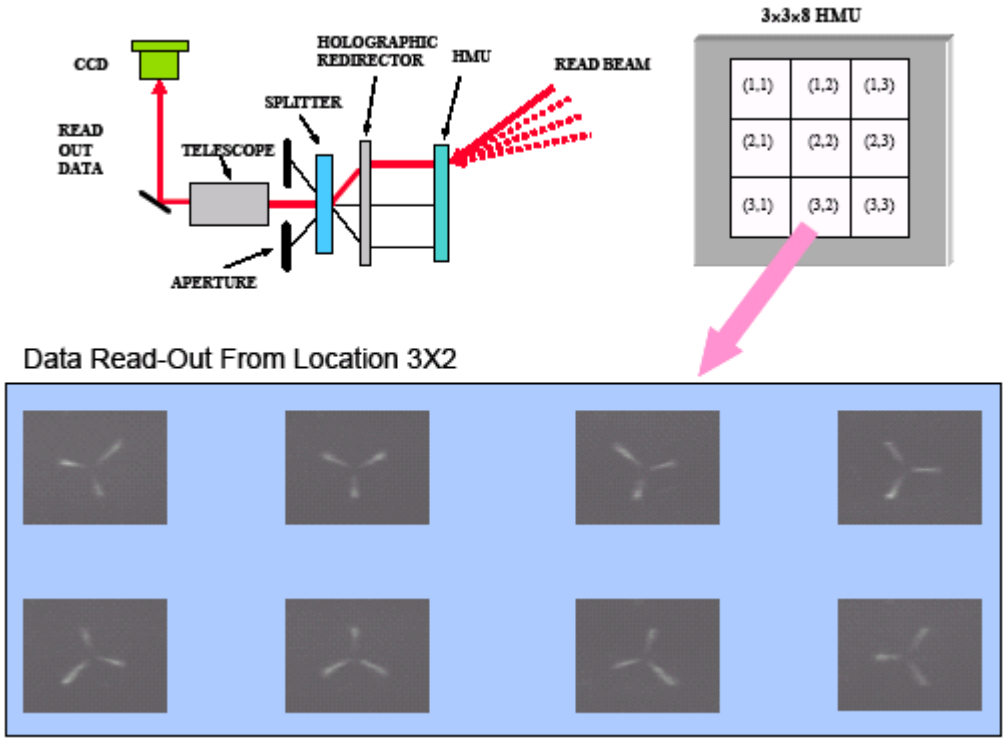

Figure 24**.** Examples of data pages retrieved through a simplified version of the SPHM architecture using a pair of galvo-mounted mirrors for deflections.

8.2 Holographic Memory with Shift-Invariant Real-Time Correlator

The diagram in Figure 25 shows our proposed system, consisting of the high capacity holographic memory coupled with a shift-invariant Fourier plane correlator. The super-parallel holographic memory is the architecture proposed by our group to implement dense SAM with fast retrieval, capable of storing over 1TB of data. A common choice for a system consisting of a holographic memory with a correlator readout is to implement the correlator in the joint transform (JTC) architecture. However,

we note that the correlation should be performed in the real-time VanderLugt correlator (VLC) architecture to achieve a much higher image recognition system operational speed. The real-time VLC shown in Figure 25 is implemented via phase conjugation in a degenerate four-wave mixing setup. The query image is transferred to the laser beam with the help of a spatial light modulator (SLM). The grating in the dynamic holographic material is written by a beam carrying the Fourier Transform of the query image and a reference plane wave. The grating is written at the speed limited by the response of the photorefractive material and the SLM operation rate, both of which are currently in the KHz range. However, once the grating for a particular query image has been written, the rest of the correlation process happens at the speed at which the probe beam diffracts from the grating, i.e., the speed of light or a THz rate. The probe beam, which is counter-propagating to the reference beam, is bearing the Fourier Transform of the filter image retrieved from the holographic memory. As described previously, the rate of information retrieval from the super-parallel holographic memory is limited by the operational speeds of the beam deflectors, and the shutter array (the rest of the components are diffractive optical elements). MEMS-based beam deflectors and shutter arrays can currently operate at MHz rates. Therefore, our proposed system can, in principle, perform image recognition by processing about a million of images per second. With the advancement of the SLM technology to megapixel capability levels, correlation performance rates of 10^{12} bps may become attainable [56]. In contrast, in a real-time JTC setup, which is also implemented by four-wave mixing, the grating would be written by the beams carrying the Fourier Transforms of the query and filter images. The probe beam would be a plane

wave incident exactly counter-propagating to one the writing beams. While searching through the holographic memory to find a match for the query image, the filter image is updated, and the grating needs to be re-written every time. This severely limits the speed of the image recognition process.

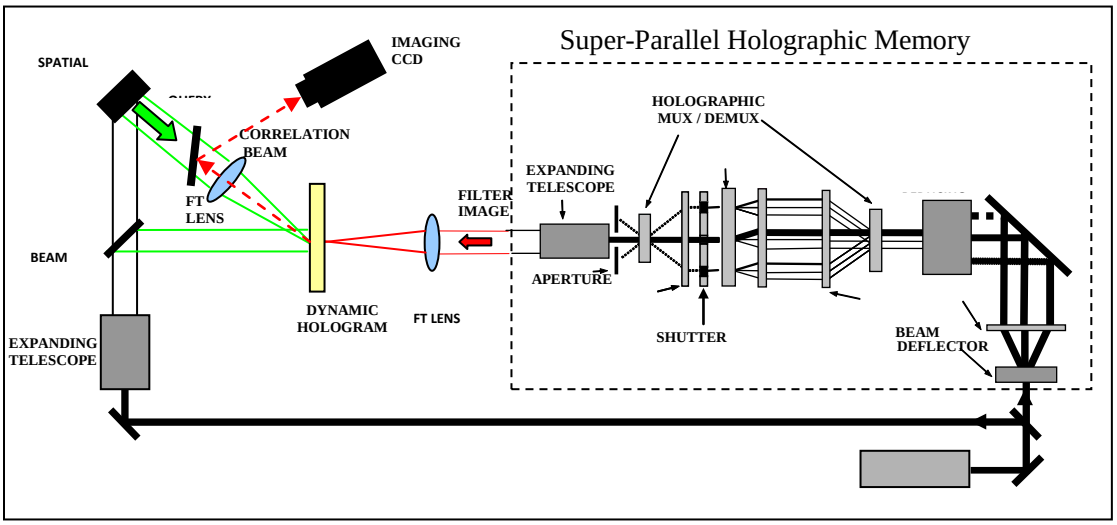

Figure 25. Super-Parallel Holographic Memory with real-time VanderLugt correlator.

9 Angular Bandwidth Study

9.1 Experimental Procedure

We studied diffraction in photorefractive polymer samples by performing incoherent phase conjugation readout in degenerate four-wave mixing configuration [57]. The diagram illustrating the experimental setup is presented in Figure 26. The experiment was performed with an ND:YAG frequency doubled solid-state pumped Verdi green laser, operating at 532nm wavelength with a linewidth of 5MHz. The photorefractive polymer

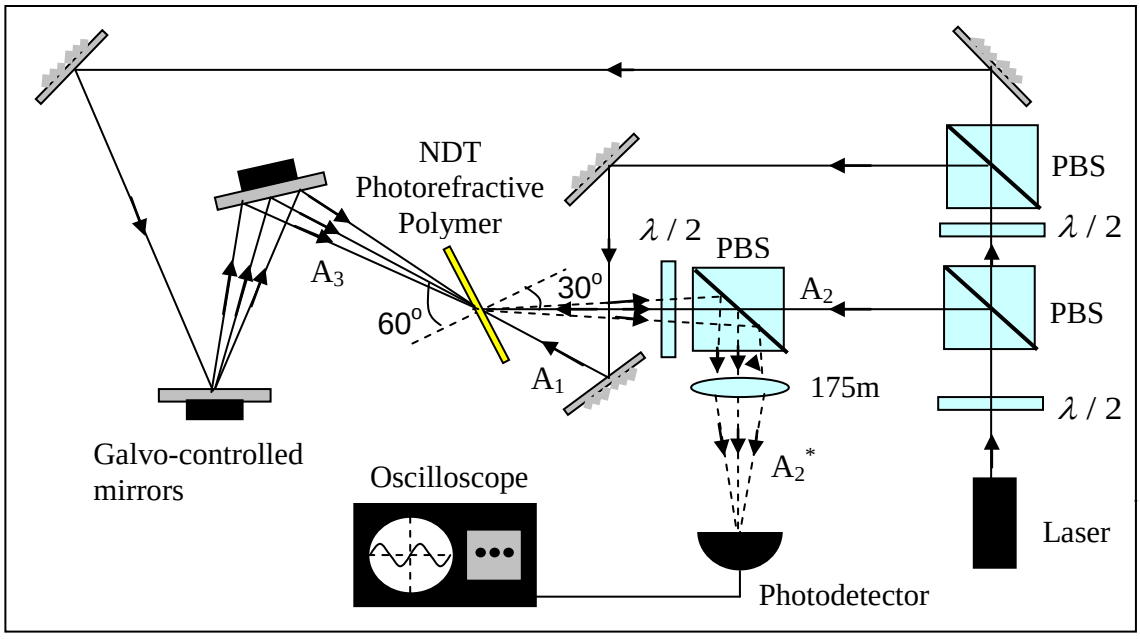

Figure 26. Experimental setup for measuring the angular bandwidth of the photorefractive polymer.

samples we obtained from Nitto Denko Technical Corp. (NDT) were 16μm, 37μm, 50μm, and 106μm thick. These samples consisted of the photorefractive polymer composite with an average refactive index n_0=1.6 sandwiched between two electrode-coated glass plates. Photorefractive polymers of a similar chemical composition but sensitized at 633nm have been recently reported in the literature [58,59]. The samples also had a large transverse active area of about 1.5" in diameter. The grating was written by two s-polarized collimated gaussian beams A_1 and A_2, incident on the hologram at 60^o and 30^o to normal in the air, respectively. Both writing beams were each 5mW in power, with spot diameters of 5mm. Because of the Fresnel refraction in glass, the actual angles of incidence of the beams A_1 and A_2 forming the gating in the material were 35^o and 20^o, respectively. The gratings were written by s-polarized, instead of p-polarized beams, in order to achieve a higher refractive index modulation depth. An asymmetric writing arrangement was needed so that the K-vector of the gratings was oriented at an angle to the z-axis, which was the direction of the poling field (see Chapter 5.7). The p-polarized probe beam A_3 at 2mW power with 5mm spot was incident on the grating, aligned to be exactly counter-propagating to the writing beam A_1. Diffraction efficiency of about 1% (higher for thicker samples and lower for thinner ones) was observed. The phase-conjugated beam A_2^* was reconstructed with p-polarization. After passing through the half-wave plate, A_2^* became s-polarized, and subsequently it was reflected by the polarizing beam splitter (PBS) cube. Note that all PBS cubes mentioned in this paper transmit p-polarized and reflect s-polarized beams. In order to produce diffraction, DC voltage had to be applied across the thickness of the sample. Typical voltage

requirements for a similar material sensitive at 633nm wavelength have been reported in previous publications. To verify the optimal voltage level for our particular experimental conditions, we have measured the diffraction effciency while linearly scanning the applied voltage at 5Hz rate. Normalized diffraction efficiency resuts for 37μm thick sample are presented in Figure 27. The maximum diffraction is obtained at 3kV external field. Although not shown in the diagram, the diffraction efficiency was observed to decrease sharply as the voltage in excess of 3kV was applied.

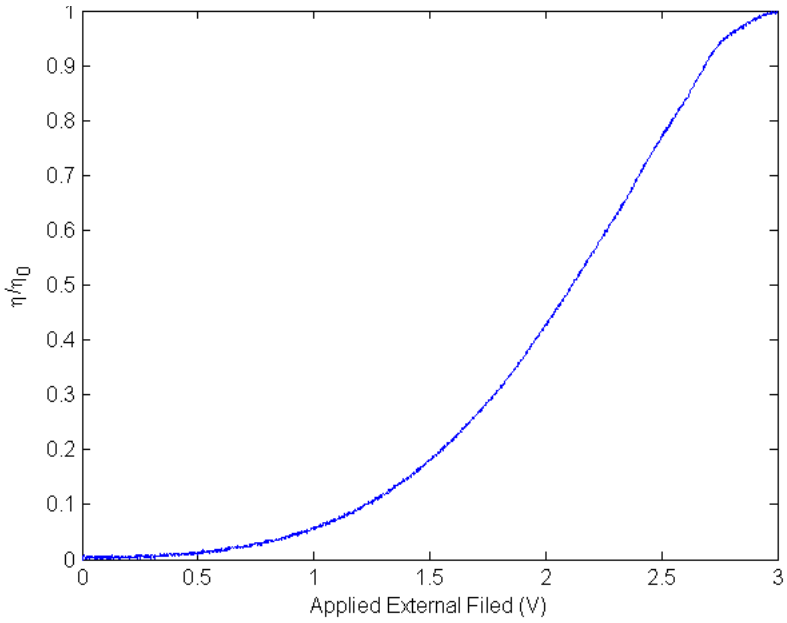

Figure 27. Normalized diffraction efficiency vs. applied voltage for 37μ thick photorefractive polymer sample

In order to measure the angular bandwidth of the photorefractive polymer samples, the probe beam was scanned with the help of computer-controlled galvo mirrors

(see Figure 2). The two-mirror galvo system, sweeping at an average rate of 15rad/s, was designed to keep the probe beam at a fixed spot on the hologram, while changing the angle of incidence. Since the phase-conjugated beam A_2^* was also sweeping through a large angle, a 2-f to 2-f single lens imaging system was set up to keep A_2^* on the detector. The phase-conjugated beam was detected with a Thorlabs PDA55 10MHz bandwidth photodetector.

9.2 Proof of Bragg Diffraction Regime

Under the stated experimental conditions we observed only the single order (Bragg) diffraction. To confirm that diffraction in our samples was in the Bragg regime, we calculate the values of $Q = \frac{2\pi\lambda L}{n_0\Lambda^2}$ and $\rho = \frac{\lambda^2}{\Lambda^2 n_0 n_1}$ parameters introduced in Chapter 3.3. We measured the diffraction efficiency for Bragg-matched incidence using the setup in Figure 26. Then, assuming that we are dealing with Bragg regime diffraction so that coupled wave theory is applicable, we calculate n_1 from the diffraction efficiency, which has the form $\eta = \sin\left(\pi n_1 d / \lambda\sqrt{c_R c_S}\right)$. We estimate that $n_1 \approx 3\times10^{-4}$ for all four samples, so that $Q \approx 20$ for the thinnest sample (16μ) and $\rho \approx 300$ for all samples. Cleary the value of Q is larger for thicker samples because Q scales linearly with length. The conclusion is that since Q > 10 and $\rho >> 1$, we are indeed dealing with Bragg regime diffraction, so that the coupled wave theory should be applicable to describing the diffraction process. The experimental measurements of the angular bandwidth along with the theoretical plots for samples of thickness 16μm, 37μm, 50μm, and 106μm

are presented in Figures 28(a)-(d). The theory plot was obtained from the coupled wave equations for lossless transmission dielectric gratings as presented in Chapter 7. An almost identical plot of normalized diffraction efficiency vs. angular displacement was obtained using the results of the volume diffraction in the Born approximation theory presented in Chapter 6.

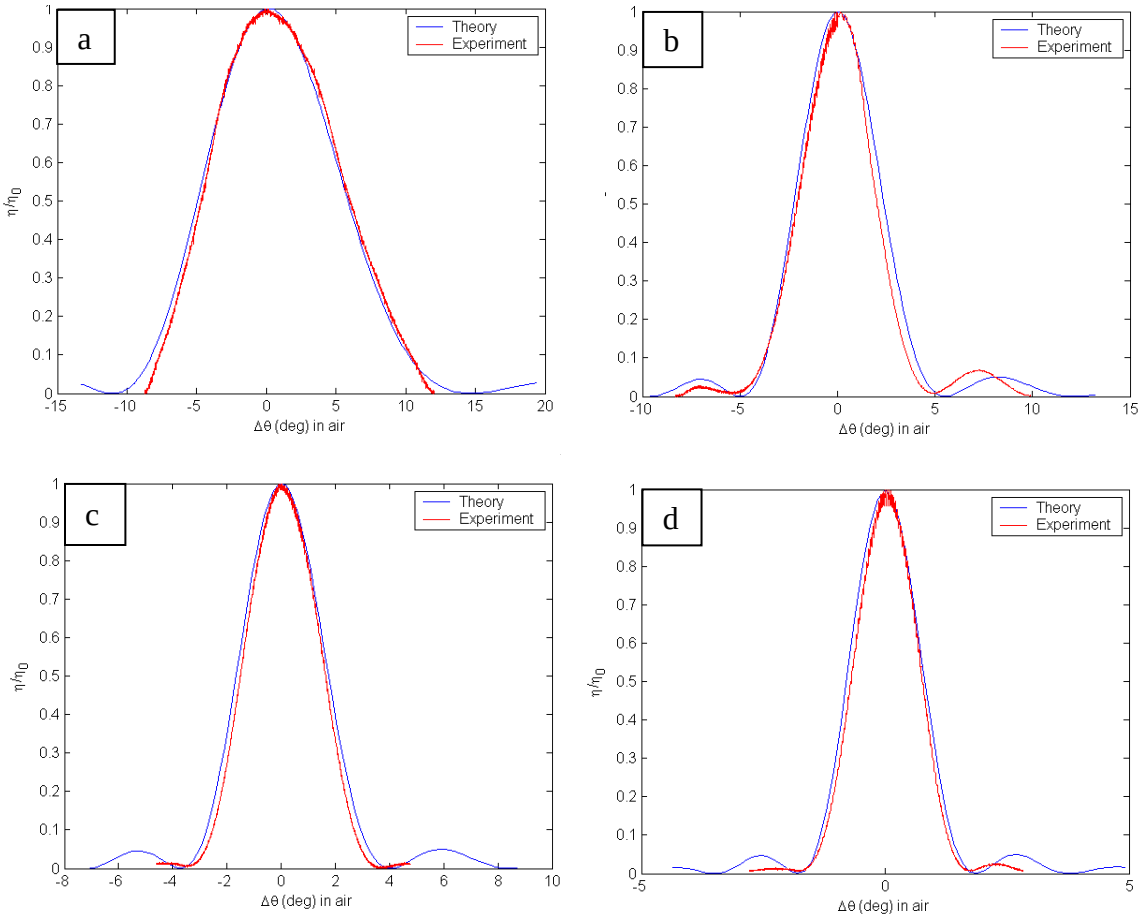

Figure 28. Normalized diffraction efficiency vs. angular deviation in air for (a) 16μm, (b) 37μm, (c) 50μm and (d) 106μm thick photorefractive polymer samples.

9.3 Direction of the Diffracted Beam

In addition, we have also performed a measurement of the angular deviation from the Bragg angle of the diffracted beam ($\Delta\theta_d$) as a function of the angular deviation of the probe beam ($\Delta\theta_p$). We used the same setup as shown in Figure 26, with the only difference that the photodetector was replaced by a ruler. We estimated $\Delta\theta_d$ by measuring the shift of the diffracted beam spot on the ruler as we changed the angle of the probe beam by a known amount. Data is presented for photorefractive polymers 16 μm (Figure 29(a)) and 37μm (Figure 29(b)) thick. The experimental data is shown with circles, while the theory curve was obtained using the *Ewald* diagram vector model (Figure 18) as presented in Chapter 6 in the context of diffraction in the Born approximation theory. All angles we measured in air. One can see that the theory is quite in a good agreement with the experiment.

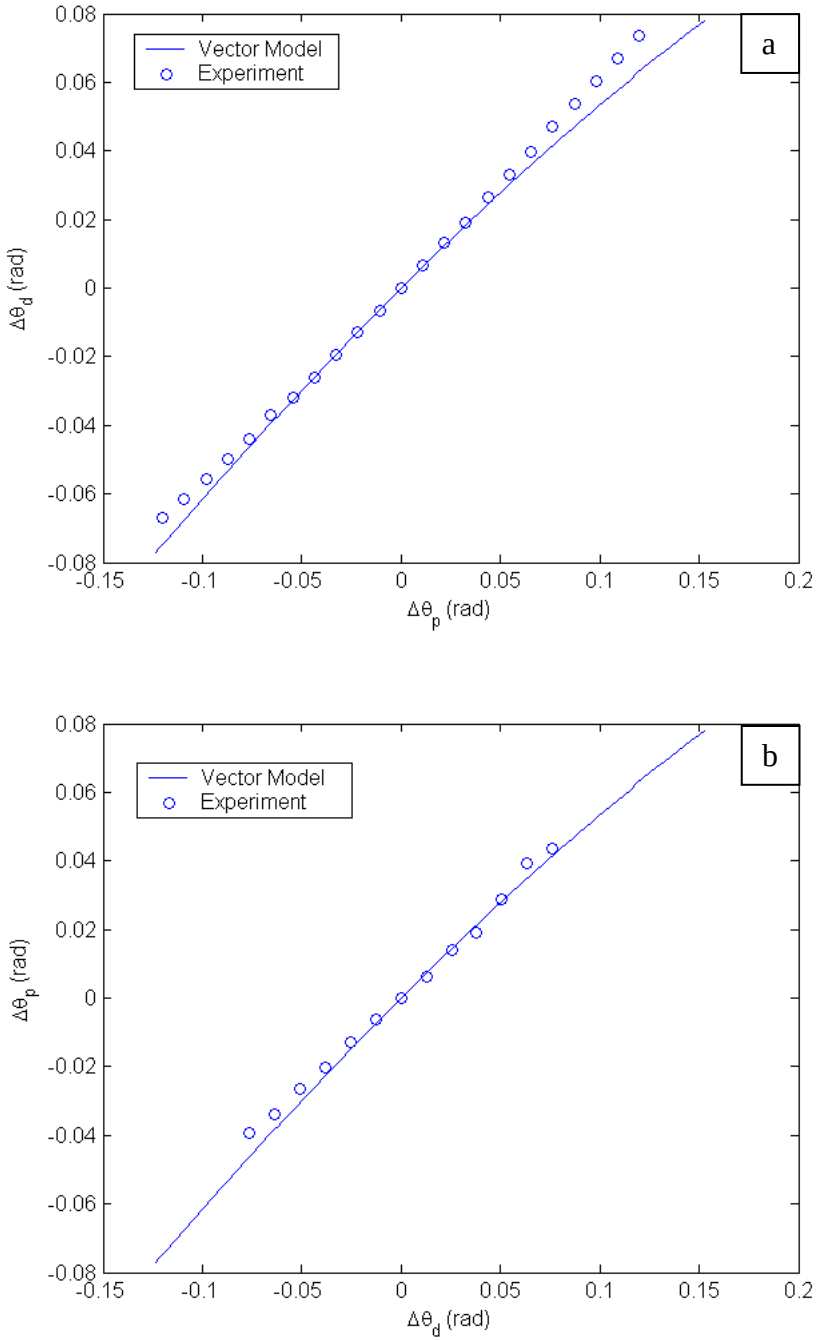

Figure 29. Angular deviation from the Bragg angle of the diffracted beam $\Delta\theta_d$ (rad) vs. the angular deviation of the probe beam $\Delta\theta_p$ (rad) in air for (a) 16μm and (b) 37μm thick photorefractive polymer samples.

10 Correlation Experiment

In this chapter we present a study of thin-film triarylamine-based photorefractive polymer composite operating at 532nm, produced by Nitto Denko Technical Corp. (NDT). We consider this material to be the prime candidate for a practical implementation of a shift-invariant VanderLugt correlator (VLC) coupled with super-parallel holographic memory [57]. Photorefractive polymers of a similar chemical composition but sensitized at 633nm have been recently reported in the literature [58,59]. A photorefractive polymer sensitive at 532nm is preferred for our project, because the Memplex® photopolymer holographic storage material [60] that we intend to use for constructing super-parallel holographic memory is also sensitive at 532nm. A real-time VLC based on photorefractive polymers operating at 633nm has been demonstrated in the past [14]. However, in this thesis we concentrate on shift-invariant property of correlation. In addition, in order to achieve edge-enhanced correlation, the experiment reported in [14] relied on cross-hairs filter to block the low frequencies in the Fourier spectrum. In our experiment, edge-enhancement was achieved in real time by adjusting the intensities of the writing beams [45,61]. Shift-invariance of correlation was a direct consequence of the thickness of the material used.

10.1 Advantage of Using This Material.

It should be noted that the large transverse area of the photorefractive polymer samples contributes to enhanced reliability of correlation. The spatial frequency components in the Fourier plane of the probe beam may be distributed over a large

area, depending on the features of the beam and the focal length of the Fourier-transforming lens. Spatial Fourier Transform of sharper images has a larger spatial area. For example, the Fourier spectrum of the MIG-25 jet image obtained from a 100x150-pixels SLM size image with a 250mm lens covered an area of about 4mm in diameter. Using the same lens, a 50x50 pixels edge-only box produced a Fourier Transform cross-section in the shape of a cross with a 1cm spread. Producing a large Fourier-plane spot is preferred because achieving a better resolution between the adjacent spatial frequencies improves the correlator performance. Therefore, it is essential to have a sample with a large cross-section area, capable of capturing the entire Fourier spectrum of the filter and query images. In addition, the real-time VLC architecture used in the experiment is quasi-phase matched, because only the mean k-vector of the probe beam (essentially only the DC part of the spectrum) is counter-propagating to the reference beam [62]. Different Fourier frequency components of the spectrum of the probe image are incident at different angles with respect to the reference. Higher spatial frequencies that carry the information about the image contours are incident at steeper angles. The larger the spatial extent of the Fourier spectrum, the larger is the angular deviation of the high spatial frequency components from the Bragg angle. Thus, the high spatial frequencies will not diffract from the grating unless their angle of incidence is within the allowed angular bandwidth. Therefore, it is very advantageous to have a real-time material that is thin and in addition has a large aperture. It would be more expensive and difficult to grow optical quality photorefractive crystals that have a comparable thickness and aperture.

10.2 Experimental Procedure

We performed the real-time shift-invariant VanderLugt correlation experiment using a 37μm photorefractive polymer sample. The diagram detailing the experimental setup is shown in Figure 30. One can see from Figure 28(b) that the angular bandwidth in the air measured between the first nulls of the sinc function for the 37μm sample is about ten degrees. This wide angular bandwidth enables the use of this material for shift-invariant correlation. Expanded laser beams with spot size of 1" diameter were used in the correlation experiment. The query image of MIG-25 jet (Figure 31(a)) was encoded on the expanded laser beam wit the help of a Boulder Nonlinear Systems 512x512 pixel reflective FLC spatial light modulator (SLM) with a pixel size 15x15μm. The filter image of a MIG-25 jet was retrieved from the Mempex® photopolymer-based holographic memory. A CCD capture of the retrieved image is shown in Figure 31(b). A real-time grating in the NDT photorefractive polymer was written with an s-polarized Fourier-transformed query image beam and an s-polarized plane wave. The probe beam carrying the Fourier transform of the filter image was p-polarized. The writing beams carried about 5mW of optical power each, while the probe beam was about 0.5mW. A quarter-wave plate and the mirror shown in the diagram in Figure 30 by dashed lines were installed on flip mounts. The purpose of these two components was to monitor the power ratio of the signal and reference beams in order to produce a grating where the DC component of the query image spectrum was not well recorded compared to the high frequencies. Since most optical power of an image spectrum resides in the low frequencies, if the intensity of high frequencies matches the intensity of the reference

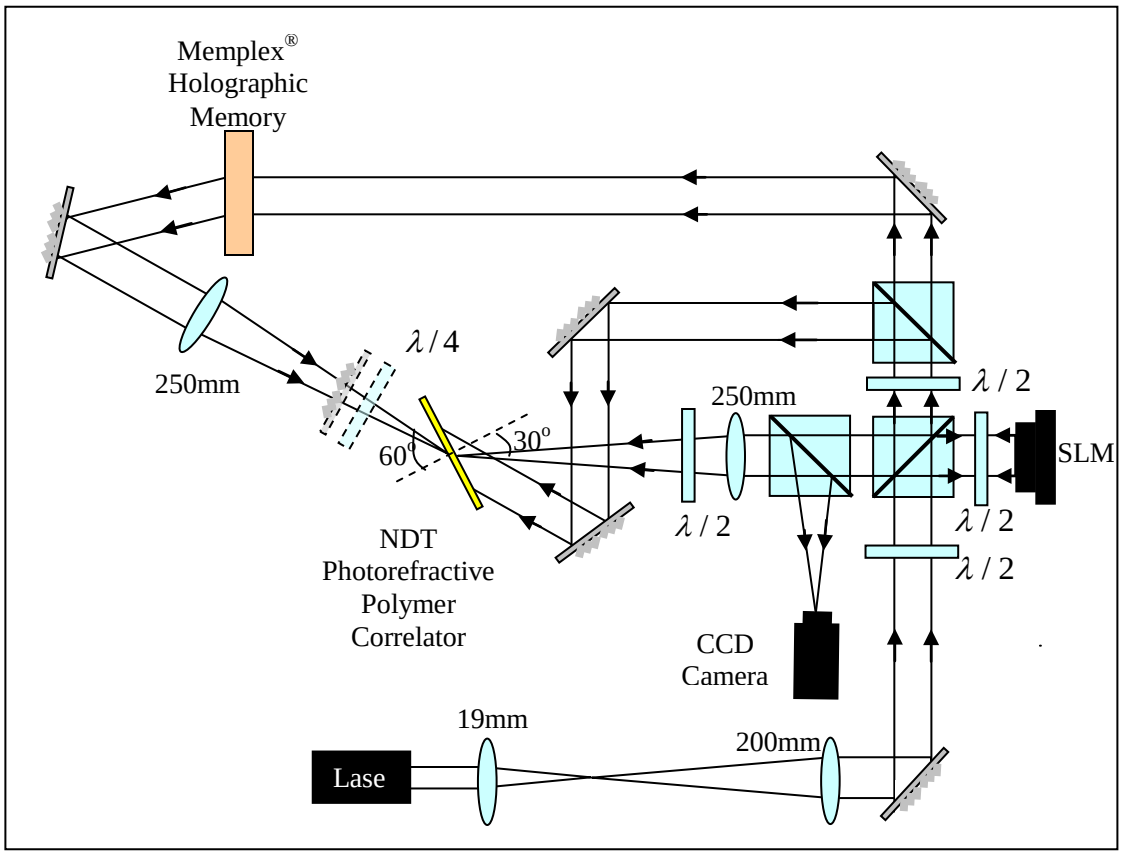

Figure 30. Experimental setup for demonstrating a translation-invariant real-time VanderLugt correlator implemented with a 37μm thick photorefractive polymer.

beam, the intensity of the DC component significantly exceeds the intensity of the reference. Hence, the modulation depth (*m*) of the DC part of the spectrum is low, and the DC is not recorded well in the hologram. DC suppression could be observed in real-time by retro-reflecting the reference beam with the flipping mirror through the quarter wave plate. Double passing of the s-polarized reference beam through the quarter-wave plate resulted in converting it to p-polarized beam. The retro-reflected reference, now acting as

a probe beam, diffracted from the grating, producing a phase conjugated beam carrying an edge-enhanced image that could be observed with a CCD camera. A CCD capture of the edge-enhanced SLM query image is shown in Figure 31(c). The image is inverted with respect to the original because the phase-conjugating system acts as a 4-f system.

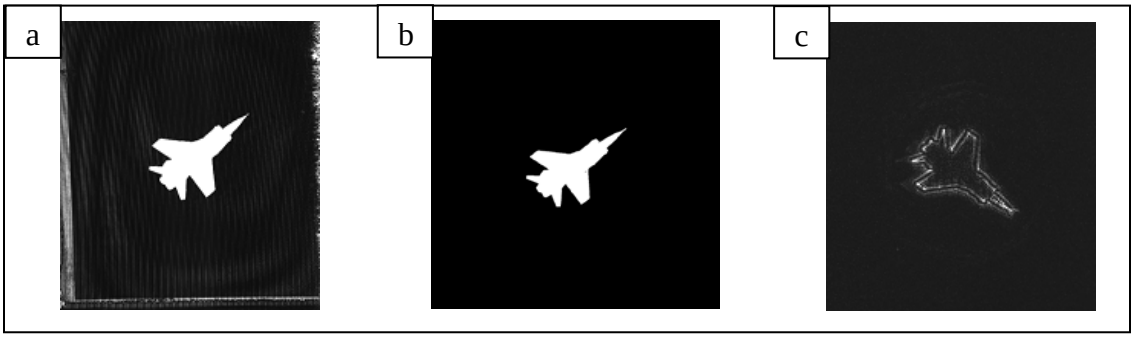

Figure 31. **(a)** Image retrieved from Memplex photopolymer memory. **(b)** SLM image. **(c)** Edge enhanced phase-conjugated reconstruction of the SLM image.

Once the desired level of edge-enhancement was achieved, the quarter-wave plate and the mirror were lowered so that the cross-correlation signal could be observed on the CCD camera. For the image in Figure 32(a), the correlation and thresholded signals are shown in Figures 32(b) and (c). We performed shift-invariant correlation by projecting from the SLM a query image of two MIG-25 jets, horizontally translated to the left and to the right by about 100 pixels in the SLM frame (Figure 32(d)). In the experimental setup with a 250mm Fourier-transforming lens, this shift corresponded to $|\Delta\theta|=0.34^{o}$ angular deviation from the Bragg angle, which is well within the allowed angular bandwidth range $|\Delta\theta_{\max}|=5^{o}$ of the 37μm thick photorefractive polymer. In fact, for the

experimental system in Figure 30, even the maximum horizontal shift from the center of the SLM by 256 pixels results in $|\Delta\theta|=0.88^{o}$. The correlation signal and the thresholded signal are shown in Figure 32 (e) and (f). Vertical displacement of the query image in the SLM plane corresponds to displacements along the Bragg degeneracy plane [63]. Therefore, shift-invariance of correlation results trivially for the image shown in Figure 32(g). The correlation and thresholded signal are shown in Figures 32(h) and (i). We observed a considerable amount of speckle noise in the correlation because of scattering in the photorefractive polymer. One would expect to obtain a much cleaner correlation signal if an optical quality photorefractive crystal was used instead. Nevertheless, the correlation signal from the photorefractive polymer could be thresholded to produce an unambiguous spot identifying the location of the query image.

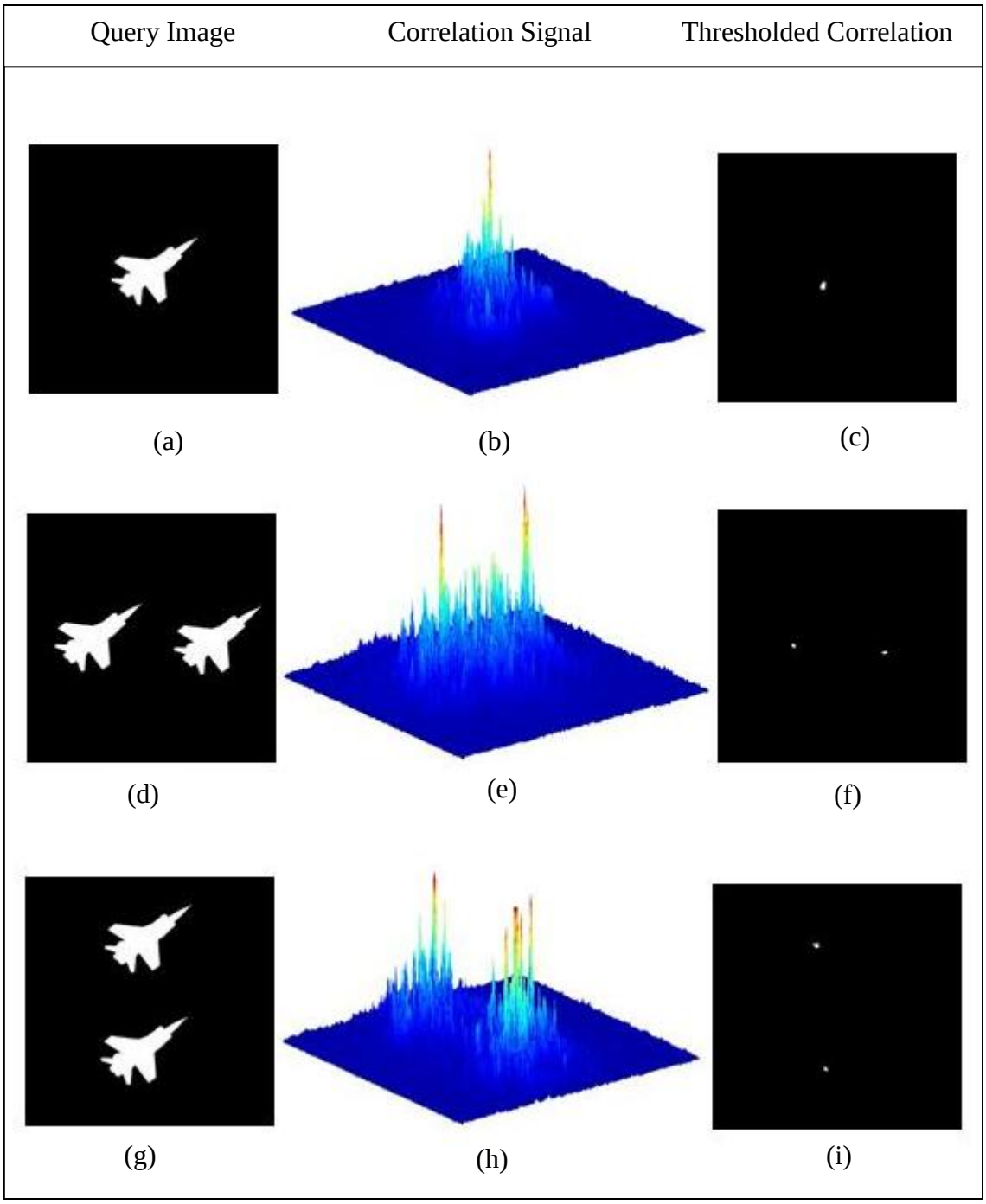

Figure 32. Correlation results. (a)-(c) autocorrelation, (d)-(f) horizontal shift, (g)-(i) vertical shift.

11 Conclusions

11.1 Summary

We have studied, theoretically as well as experimentally, diffraction from volume holographic gratings, and its application to design of optical image recognition system. We have proposed a holographic system for image recognition in real time by implementing a time-efficient exhaustive search in a very large image database with a shift-invariant correlator. The database of filter images contains multiple copies of the same image to account for rotation and scale variance, while shift invariance is accomplished by using a thin correlator material. The filter images are to be stored in the ultra-high density spatio-angular multiplexed holographic memory with nearly 2TB storage capacity. Real-time recognition of the stream of the incoming query images is to be performed with a photorefractive holographic correlator. Time-efficient search is accomplished if one uses a real-time VanderLugt correlator, because this architecture allows to overcome the speed limit of the photorefractive gratings formation. We have identified photorefractive polymers that can be made as thin as 16μm, and as consequence posses a large degree of shift-invariance, to be the best materials for constructing our system. Photorefractive polymers we discovered 15 years ago, and their properties are currently under active investigation. We performed a series of experiments to measure the angular bandwidth of these materials in the degenerate four-wave mixing architecture, as well as demonstrated shift-invariant correlation in the real-time VanderLugt architecture. We have shown that

We have also investigated the two main theories that explain diffraction from

volume holographic gratings: diffraction in the Born approximation and coupled-wave theory. Both theories analyze generic volume gratings without taking material properties into account, with the assumption of weak modulation. Until now, both theories we believed to produce equivalent results. The first theory is based on the integral approach. Diffraction is formulated as a scattering from a grating-induced potential. A series expansion in integrals follows, with all higher orders neglected because of the assumed weak modulation. We showed that the results for off-Bragg readout that follow from the Born approximation theory are consistent with conservation of energy and momentum laws. The second theory is based on differential equations approach. A system of two coupled differential equations is derived from the Helmholtz equation by keeping only the first diffraction order and making the slowly varying envelope approximation. We showed, for the first time, that the results for the wave vectors of the diffracted and transmitted beams are not consistent with the conservation with energy and momentum conservation laws. We also showed that an existing alternative formulation of the coupled wave theory, where a mismatch vector is assumed, also does not lead to correct results.

11.2 Future Work

The photorefractive polymer-based VanderLugt correlator system that we described in this thesis needs several improvements before it can become a working device. A diffraction efficiency of 1% that we reported for the experiment may be insufficient in operation of this correlator with the super-parallel holographic memory

(SPHM). In the current SPHM design, the output beam the output beam is very weak (μW or even nW regime). Therefore, the speed of the correlation signal detection will be limited by the diffraction efficiency of the correlator because of the noise floor of the detector. One way to increase the diffraction efficiency of the correlator is to use a probe beam at a different wavelength, which is outside of the material response bandwidth. In degenerate four-wave mixing setup that we used in the experiment, the probe beam is cross-polarized to, and hence non-interacting with the write beams. However, the probe beam partially erases the grating because the material is sensitive to the probe beam wavelength.

Although we presented the arguments that the coupled wave theory produces results that are not consistent with conservation of energy and momentum, we do not explain the origins of this error. One way to find an explanation would be a step-by-step comparison the Born-approximation diffraction and the coupled wave theories. Since one theory is integral-based, and the other is differential equations-based, both theories need to be reformulated either in integral or in the differential equations form.